PURDUE UNIVERSITY
GRADUATE SCHOOL
Thesis/Dissertation Acceptance

This is to certify that the thesis/dissertation prepared

By _Amritanshu Palaria_

Entitled
Multi-scale Predictive Modeling of Nano-material and Realistic Electron Devices

For the degree of ____Doctor of Philosophy____

Is approved by the final examining committee:

Gerhard Klimeck
_____
Chair

Mark S. Lundstrom

Supriyo Datta

Alejandro Strachan

To the best of my knowledge and as understood by the student in the *Research Integrity and Copyright Disclaimer (Graduate School Form 20)*, this thesis/dissertation adheres to the provisions of Purdue University's "Policy on Integrity in Research" and the use of copyrighted material.

Approved by Major Professor(s): Gerhard Klimeck

Alejandro Strachan

Approved by: Michael R. Melloch   12/09/2010
_____
Head of the Graduate Program   Date

PURDUE UNIVERSITY
GRADUATE SCHOOL

Research Integrity and Copyright Disclaimer

Title of Thesis/Dissertation:

Multi-scale Predictive Modeling of Nano-material and Realistic Electron Devices

For the degree of _____Doctor of Philosophy_____

I certify that in the preparation of this thesis, I have observed the provisions of *Purdue University Executive Memorandum No. C-22,* September 6, 1991, *Policy on Integrity in Research.**

Further, I certify that this work is free of plagiarism and all materials appearing in this thesis/dissertation have been properly quoted and attributed.

I certify that all copyrighted material incorporated into this thesis/dissertation is in compliance with the United States' copyright law and that I have received written permission from the copyright owners for my use of their work, which is beyond the scope of the law. I agree to indemnify and save harmless Purdue University from any and all claims that may be asserted or that may arise from any copyright violation.

Amritanshu Palaria
_____
Printed Name and Signature of Candidate

12/09/2010
_____
Date (month/day/year)

*Located at http://www.purdue.edu/policies/pages/teach_res_outreach/c_22.html

MULTI-SCALE PREDICTIVE MODELING OF NANO-MATERIAL AND

REALISTIC ELECTRON DEVICES

A Dissertation

Submitted to the Faculty

of

Purdue University

by

Amritanshu Palaria

In Partial Fulfillment of the

Requirements for the Degree

of

Doctor of Philosophy

December 2010

Purdue University

West Lafayette, Indiana

TABLE OF CONTENTS

LIST OF TABLES

LIST OF FIGURES

ABSTRACT

Palaria, Amritanshu. Ph.D., Purdue University, December 2010. Multi-scale Predictive Modeling of Nano-material and Realistic Electron Devices. Major Professor: Gerhard Klimeck.

Among the challenges faced in further miniaturization of electronic devices, heavy influence of the detailed atomic configuration of the material(s) involved, which often differs significantly from that of the bulk material(s), is prominent. Device design has therefore become highly interrelated with material engineering at the atomic level. This thesis aims at outlining, with examples, a multi-scale simulation procedure that allows one to integrate material and device aspects of nano-electronic design to predict behavior of novel devices with novel material. This is followed in four parts:

1. An approach that combines a higher time scale reactive force field analysis with density functional theory to predict structure of new material is demonstrated for the first time for nanowires. Novel stable structures for very small diameter silicon nanowires are predicted.

2. Density functional theory is used to show that the new nanowire structures derived in 1 above have properties different from diamond core wires even though the surface bonds in some may be similar to the surface of bulk silicon.

3. Electronic structure of relatively large-scale germanium sections of realistically strained Si/strained Ge/ strained Si nanowire heterostructures is computed using empirical tight binding and it is shown that the average non-homogeneous strain in these structures drives their interesting non-conventional electronic characteristics such as hole effective masses which decrease as the wire cross-section is reduced.

4. It is shown that tight binding, though empirical in nature, is not necessarily limited to the material and atomic structure for which the parameters have been empirically derived, but that simple changes may adapt the derived parameters to new bond environments. Si (100) surface electronic structure is obtained from bulk Si parameters.

1. INTRODUCTION

1.1. Device challenges at nano-scale

The transistor has undergone drastic evolution in the past seven decades. From the very simple germanium crystal sitting on two gold foils developed at the Bell Labs to the modern nanometer CMOS, it has been an amazing journey guided by the principle that integrated circuits should double their density every 18 months, the so-called Moore's Law. Over the years, it has become increasingly clear that manufacturability and operation of the device do not alone determine its success or even viability in the highly competitive industry. As device sizes shrink, requirements of low power, high performance and high reliability have become increasingly important. Today we stand at a juncture where some characteristic sizes in transistors are nearing atomic dimensions and the design and fabrication of electronic devices and circuits poses new challenges.

1.1.1. Materials and nanoelectronic devices

Design of novel nanoelectronic devices is challenging because it requires one to take into account not only the device level quantum effects due to miniaturization, but also the changes in properties of the material itself, which can once again be explained by quantum mechanics. A very good example in this regard is provided by carbon, the group IV material just above silicon in the periodic table. Depending on its molecular structure, pure carbon can range from being a pure insulator (diamond) to semiconducting (some nanotubes), metallic (some other carbon nanotubes, graphite) and almost superconductor (graphene). Scientists have achieved the graphene transistor, which is only one atom thick and ten atoms wide.[1] While owing to challenges in fabrication and manufacture, such a transistor is far from production yet, its demonstration is a clear indicator of two characteristics of the future semiconductor devices: (a) the nature and properties of the material used for these devices would play a significant role in their properties and hence there is a constant push to find new materials with desired properties, and (b) the atomistic dimensions of the devices would make an atomistic analysis of their behavior inevitable.

Consequently, the atomic-level effects of any deviations from the ideal bonding environments observed in bulk material would have to be taken into consideration because these effects, while sometimes negligible or treated in an abstract fashion for larger devices, are expected to become proportionately large at small device dimensions.

One must also note that the interplay between materials and devices is a two-way process: not only are the new device designs motivating the search for new materials, but also the development and characterization of new materials and the technology to process them is influencing device and architecture design. A more contemporary example of the effect of new structured material concepts on device, process and architecture design is the field programmable nanowire interconnect [2], a variation of the field programmable gate array, which utilizes 15nm wide crossbar nanowires with 45nm half-pitch CMOS to "increase the effective transistor density, reduce power dissipation and dramatically improve tolerance to defective devices." [3] So we conclude that we need to carry out a full range analysis, right from the atomic arrangement in the material to transport characteristics of the full device, not only for future nano-scale devices but also to fully explore and understand the behavior of current and near future devices, which are relatively large sized, through what could be termed 'bottom up' approach in analysis and design.

1.1.2. Future of semiconductor devices

There are several different technologies being currently investigated for the future devices of the semiconductor industry. International Technology Roadmap for Semiconductors (ITRS) 2007 [4] represents the current and prospective future technologies at the various abstraction levels: state variable, material, device, data representation and architecture. While some of the technologies might require a drastic change in the fabrication processes and the manner in which devices and circuits are conceived and might therefore be a multitude of years away from large scale commercial production, there are other devices and technologies which require changes either already on-going in the industry or that are not that drastic and hence not very far from being put to actual commercial uses. Among these the foremost (according to the ITRS) are the extensions to the commercial CMOS that are currently being considered. Two such major extensions are:

1.   Ge and III-V compound channel FETs

2.   1-D nanostructures - Nanowire FETs, carbon nanotube FETs, nanowire heterostructures: The case studies in this thesis cater to this section of devices.

Today, silicon nanowires can be fabricated with good precision [5] and several devices made of them have been demonstrated in the lab. The nanowire FET,[6, 7] consists of the NW channel surrounded by an insulator (SiO_2 or HfO_2 for Si nanowires and ZrO_2 for Ge wire), gated by degenerate Si and metallic source/ drain electrodes (Au/Al or SiTi for Si nanowires and Ti for Ge nanowires). The use of B doped Si NW array [8] yields high mobilities and low subthreshold swing values, resulting in low off-currents, good on-currents and hence high on/off current ratios. Leiber's group has also produced integrated interconnect/ contact Si nanowire FETs using selective transformation of SiNWs into NiSi NWs to yield NiSi/Si/NiSi junctions.[9] Other device concepts implemented from nanowires [10] include passive diode structures consisting of crossed p- and n- type nanowires, active bipolar transistors consisting of heavily and lightly doped n- type nanowires crossing a common p-type nanowire base and complementary inverter structures assembled from n- and p-type nanowire structures.

It is important to mention that while the discussion here has been focusing on continuing Moore's law, nano-scale transistors for electronics applications are not the only possible uses of silicon nanowires. Among other applications of silicon nanowires include chemical/ bio sensors,[11] photovoltaic devices, thermoelectric devices and battery electrodes.[12]

Among other nano-materials which exhibit special properties not seen in bulk material, carbon nanotubes (CNTs) deserve a mention here, not only because they are also 1-D materials but also because semiconducting carbon nanotubes hold the promise of providing high performance FETs owing to their unique electronic structure, reduced carrier scattering (long mean free path) and hence mobilities and transconductances that meet or exceed the best semiconductors.[13] Another advantage of using CNTs is that metallic carbon nanotubes hold the promise to play the role of a low loss interconnect. On the other hand, CNTs suffer from experimental challenges such as repeatable fabrication/ isolation of one-type CNTs and doping control. Repeatable fabrication of silicon nanowires with control over orientation and size has been demonstrated and there is a lot more knowledge about silicon than carbon in the semiconductor industry. One of the things theoretically explored in this thesis is the properties of 1-D silicon nanostructures as the diameter becomes very small (<1nm). Since such structures are only recently becoming possible in the lab and very little is know about them, a theoretical study can help us know

of novel effects if any that can show up at such small diameters and can therefore act as very useful indicators to experimentalists of the utility of attempts at their fabrication.

Another design for the nanowire FET [14] uses the Ge/Si core-shell nanowire heterostructure to provide clean 1-D hole-gas and uses high-k dielectric (HfO_2 or ZrO_2) for enhanced gate coupling. This has been shown to possess high performance scaled transconductance and on-current values, which are comparable to similar length CNT FETs and substantially better than scaled planar MOSFETs. Yet another 1-D nanostructure design that can combine confinement properties of 1-D nanostructures and strain induced properties of heterostructures is the <100> strained Si/ strained Ge/ strained Ge hetero-structure nanobars or nanowires as shown in fig. 1.1.[15, 16] Some electronic effects of structural and strain engineering on this structure shall be investigated later in this thesis.
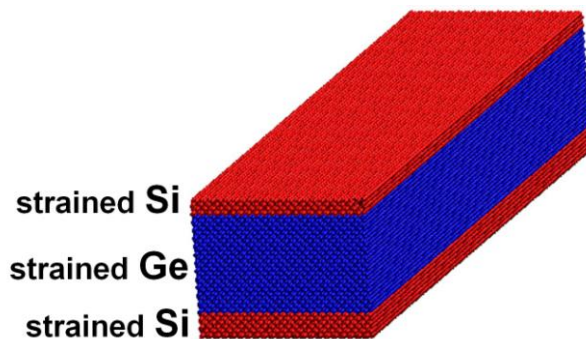
Fig. 1.1 <100> strained Si/Ge/Si nanobars studied in chapter 5 of the thesis

1.2. Predictive modeling and simulations at nano-scale

1.2.1. Predictive theory and simulation

While theoretical science serves the purpose of logically explaining experimental observations, its most attractive attribute to mankind has been its predictive power, which also guides the attainment of desired attributes of engineered devices. To explain complex observations or phenomena, one follows the reductionist approach, where one breaks down the complex problem into simpler parts and uses established theory or develops new theory to explain each of them. Conversely, one may use established (or empirically verified) theory(ies) to logically build up to a far conclusion and predict phenomena. These predictions can then be validated through a designed experiment and if needed, the theory is revised to match the actual observations.

As science and technology has grown over the centuries, 1) more complex and mathematically involved theories have propped into existence, and 2) the nature of the engineering and science problems to be dealt with has became more complicated. Both of these have led to an ever-increasing difficulty in handling the problems analytically as well as experimentally, and today the computer is heavily employed to carry out relatively quicker numerical calculations for theoretical problems of all sorts, by either first creating an appropriate computer model for the problem or directly employing the computer to solve the existing mathematically complex and otherwise insolvent theory equations and make useful predictions. In the broad area of material science and engineering, simulations have become an indispensable component of research, even replacing experiment, partly because experimental measurements are indirect and require theoretical interpretation, and partly because often the technological limitations do not allow one to perfom the ideal experiment. Computer simulations are fast developing into the third pillar of science and engineering either by acting as true first-pass experiment replacement or an indispensable aid to rationalist deduction, theoretical model verification, and design of complex engineered systems.

1.2.2. Simulation challenges in nano-scale materials and devices

A strategic challenge for nanoelectronic devices is the development and wider use of simulation techniques and procedures that bring the material and electrical communities together.

1.2.2.1. Multi-scale simulation for nano-electronic devices

Nanoscience and technology is one area that has increasingly seen the need for computer simulations, thanks to quantum theory, which, while on the one hand, provides a first principles description of materials and is therefore general and applicable to any material, on the other, possesses such a high mathematical complexity that it makes certain problems, e.g. handling of the quantum description of large multi-electron system, analytically impossible. Paul Dirac stated, "the fundamental laws necessary for the mathematical treatment of a large part of physics and the whole of chemistry are thus completely known, and the difficulty lies only in the fact that application of these laws leads to equations that are too complex to be solved." So if the problem involves a large and complicated material or device, which is often the case for realistic systems, the accurate quantum mechanical description cannot be applied with its full vigor for most

materials & devices of interest and there arises the need for multi-scale simulation. Scientists have designed empirical (and hence less general) and approximate methods such as tight binding and empirical force fields for large-scale molecular dynamics to tackle large systems or large event times for dynamics problems.

If we take a more traditional view, the electrical engineering and material science communities have used two different paths of simulation methods at the various scales, as shown in figure 1.2. This diversion of paths has to do with the nature of the problems the two communities handle. Material scientists are often more concerned with the composition and properties of materials while electrical engineers focus on the dynamics of charge transport. There has always been communication between the two through parameters derived on one side and communicated to the other. For example, the electronic band-gap and effective masses used with Boltzmann transport equation are obtained from the bandstructure calculated using density functional theory (DFT) and GW approximation. At the nano-scale however, localized changes in the electronic wave-function become important and the incorporation of atomic-scale material variations and use of a quantum transport theory like NEGF becomes necessary. At this scale, therefore, as already described in section 1.1.1, material and device design are highly inter-related and one needs a well-defined procedure to explore the structure and the properties of the devices.
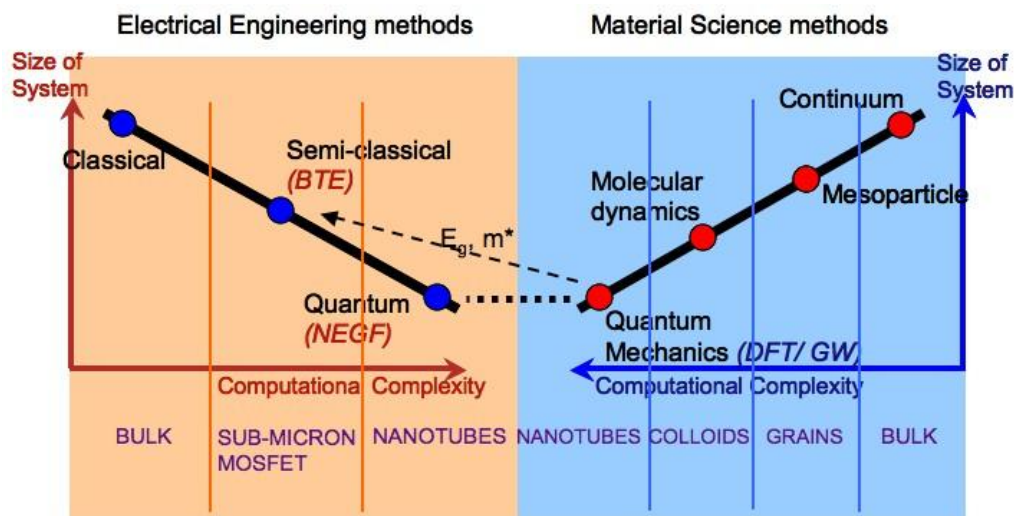
Fig. 1.2 Multi-scale simulation in electrical and material engineering communities

One point to note here is that as the science theory or method used for simulations moves down the complexity axis (reducing computational time and cost) and up the simulation size axis (or - for dynamical problems - the simulated time axis), it also loses

accuracy and generality/ transferability. Here good software engineering can help ease out the trade off. Use of parallel programming and efficient algorithms allows the use of more accurate and general scientific theories even for bigger systems. It must be noted that developing a most general program that can be applied to several problems may initially take high time and cost but will have greater returns in the long run. Sometimes, however, the programmer may, in the interest of time and effort, forgo a certain amount of generality when developing the program.

Let us consider a generalized two terminal device shown in figure 1.3. If one was to use the NEGF approach to obtain transport characteristics of this device, one would need to provide an accurate description of the channel in terms of the device Hamiltonian. One can obtain channel material structure at the atomic level (including all bond lengths and bond angles) from DFT or MD or both. For bulk-like channel materials, empirical tight binding provides an easy way of formulating this Hamiltonian. However, if the channel region carries important non-bulk bonds like defects, surfaces or interfaces, the same bulk TB parameters can no longer be used to model the channel and one needs to modify them to model these atomic level changes correctly.
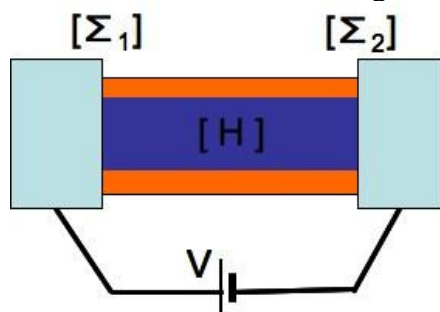
Fig. 1.3 Generic device: the channel should take structural anomalies of the material into account

So this work envisions the following multi-scale simulation approach (see fig. 1.4) to investigate transport in realistic nano-electronic devices (while the methodology described here is generally applicable, the focus of this work is on silicon and germanium materials):

1.   The structure of the nano-material, if unknown, is deduced from an integrative approach using molecular dynamics and density functional theory. This is a key step in discovery/ design of new materials and material oriented devices. Once the atomic structure of the material is well-defined, one of the atomistic simulation methods can be applied to investigate the properties.

2.   The electronic structure is obtained using extended orthogonal $sp^3d^5s^*$ tight binding using empirical parameters for bulk silicon. It will be shown in chapters 5 and 6 that the bulk parameters may need to be modified to simulate realistic structures. In this thesis, results for Si (100) surfaces are reported and compared with the electronic structures obtained from density functional theory using local density approximation (LDA) and GW correction.

3.   The Hamiltonian determined in step 2 can also be used in the standard non-equilibrium Green's function (NEGF) approach to obtain transport characteristics of the nano-device.
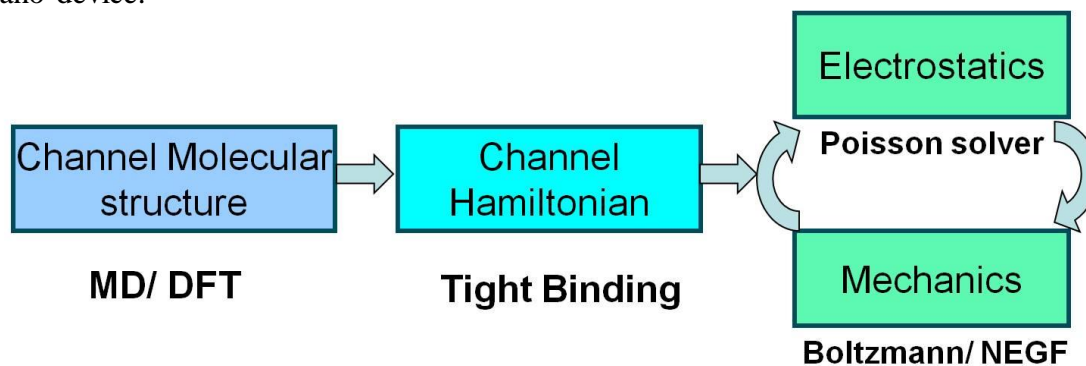
Fig 1.4 Envisioned scheme to simulate nanoelectronics bottom up taking into account material structure

1.2.2.2. Modeling of excited electronic states of materials

Among the various challenges in the field of simulations for the semiconductor industry, the 2007 ITRS lays down the challenge of improving *ab initio* modeling to provide better understanding of the physical mechanisms and interpretation of the metrology for nanoscale structures. A key problem here is that frequently for electronic material and device behavior investigation, the simulation of excited states is necessary but not possible with the state-of-the-art tools for realistic size devices, which are often much up scale than what the complex excited state theories (such as DFT with GW correction) can handle. This thesis will propose an adaptive tight binding model to simulate reasonably accurate excited states for any general material. This will be described in chapter 6.

1.3. Outline of the thesis

This thesis will describe the above discussed procedure for simulating a nano-scale electronic device. At every step, there would be a case study to apply the method to investigate new materials/ devices. Chapter 3 describes the use of reactive force field molecular dynamics and ab-initio density functional theory to predict new nano-material. The material investigated is sub-nanometer 1-D silicon nanostructures. The study described shows that hollow tubular silicon nanowires are energetically the best 1-D nanostructures for very small diameters. Chapter 4 describes the use of density functional theory to obtain the electrical and mechanical properties of these tubes. Since these structures are a more distant possibility, chapter 5 shifts to a more realistic and contemporary material, strained Si-strained Ge-strained Si nanobar, whose predicted atomic structure from reactive force field has already been verified against fabricated structures. A tight binding treatment studies the electronic band-structure of these nanostructures. Passivated, relaxed and non-reconstructed structures are strategically chosen in Chapter 5 because contemporary tight binding with bulk sp^3d^5s* parameters (used in this thesis) fails to capture the effects of reconstruction correctly. Chapter 6 then proposes the adaptive tight biding model to capture reasonably well the role of such non-bulk bonding environments as surfaces on electronic bandstructure.

2. REVIEW OF COMPUTATIONAL METHODS

This chapter will provide a brief overview of the relevant computational science and engineering methods. Most of these methods are in wide use. The following chapters will depict how these methods have been employed in this thesis. All references to the method sources shall be made in the following chapters.

The Born-Oppenheimer Approximation assumes the ions statically fixed in space (owing to their >2000 times the mass of electron) when dealing with electrons, thus allowing separation of ionic and electronic degrees of freedom when working with a solid/ liquid system.

Even after separating ions out from the variable space, the problem still remains computationally challenging in its fundamental wavefunction representation. E.g. if we consider a system with 7 ions and 4 electrons per atom, we have total 28 electrons, each being represented by its three-dimensional position vector and a single spin coordinate, the electronic wavefunction lives in 28*4=112 dimensional space! This implies that even if we use only 10 points to grid each spatial axis, we have 1084 * 228 points in the full search space.

2.1. Density Functional Theory

The dimension problem is solved, at least for reasonably sized structures, by the application of density functional theory which basically states that for a many-electron system, electron density is unique to the system with a specified external potential and therefore all system observables can be obtained as functionals of this unique density. Hence instead of working with wavefunctions living in 4n (where n = number of electrons) dimensional space, one works with the system density living in only four dimensional space (3 spatial coordinates plus 1 spin coordinate).

2.1.1. Kohn-Sham Approach

In the Kohn Sham approach, the actual many-electron system of interacting electrons is replaced by an equivalent non-interacting system which has the same density as the actual system. The interacting part of the kinetic energy and the exchange and correlation interactions among electrons are absorbed into the exchange-correlation functional of density. This allows solving for the density of the non-interacting system (the eigenstates of which are called the Kohn Sham states) through a self-consistent iterative process. Thus, the Kohn Sham approach to density functional theory provides us with the exact density of the interacting system but not the exact eigenstates of the actual system.

Actual interacting system   Non-interacting system

Same $\rho(r)$

$$H[\rho] = T[\rho] + V_{ext}[\rho] + U_{ee}[\rho]$$

$$U_H[\rho] + U_{xc}[\rho]$$

$$H^{KS} = -\frac{h^2}{2m}\nabla^2 + v_R(\vec{r})$$

$$v_R(\vec{r}) = f[V_{ext}(\vec{r}), \rho(\vec{r}), U_{xc}[\rho](\vec{r})]$$
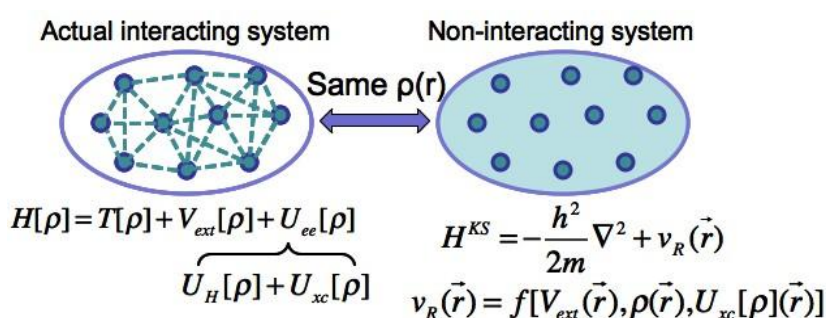
Fig. 2.1 The Kohn-Sham approach to DFT

2.1.2. Exchange-correlation functionals

Two common exchange correlation functionals in use for DFT calculations are the local density approximation (LDA) and the generalized gradient approximation (GGA).

The general trends are:

1.   GGA improves cohesive energies.
2.   GGA improves bond lengths and bond angles.
3.   GGA slightly improves the gap energy and the dielectric constant.
4.   LDA gives poor electronic densities of atoms in the core region where the electrons are quite localized.

2.2. GW Approximation

The Kohn-Sham approach is unable to correctly provide the excited state energies because the Kohn Sham orbitals are not the actual single electron states of the interacting

system (Kohn Sham theory, however, describes the filled electron states quite well). To handle the excited states of the system, different methods in use are:

Time dependent density functional theory

Many body perturbation theory (in the GW approximation)

Non equilibrium Green's function (NEGF) for transport

This thesis will make use of GW results as the bench mark for other electronic structure calculations. GW is a Green's function method based on the fact that the poles of the Green's function of a system represent its eigen-energies. However, for a multi-electron system, the single state energies actually represent the difference between multi-state energies and since the N electron eigenstates are not also the eigenstates of the N+1 electron system, one needs an energy-dependent self-energy correction to the Hamiltonian (representing interaction with other particles) and this leads to a Dyson like recursive equation for the Green's function where the self-energy acts like a perturbation in the interaction picture. The GW approximation is characterized by the use of the product of the Green's function G and the dynamically screened Coulomb interaction W to represent the self-energy. The single particle states from GW are thus each the state of an electron with the surrounding hole region which screens it, the so-called quasiparticle. The use of GW approximation is obviously a self-consistent iterative process. The starting states for the application of GW are often the DFT-LDA or GGA single electron states. However, due to its complexity GW is highly demanding on the computational resources and not scalable to larger systems.

2.3. Molecular Dynamics

The SCF iterations to solve for the electronic energy in a system with fixed ions make the DFT simulations tedious. The relaxation of a system in DFT when the number of ions exceeds about 1000 becomes highly demanding of computational resources. In order to simulate large systems, scientists have developed interatomic potentials or force fields that describe the interaction between atoms without resorting to an electronic structure calculation. The generalized force field with atom- or bond- specific parameters models the interactions among the electrons and ions as a function of atomic positions and thus relieves dependence of the total energy on electronic variables. The use of an algebraic expression to get the internal forces instead of the self-consistent iterations required for DFT leads to considerable savings in terms of computational time and resources. This in

turn allows the simulation of large systems and long dynamics. Thus the method of molecular dynamics enjoys the advantages of low complexity, less time and higher scalability over *ab initio* methods.

2.3.1. Reactive force fields

Reactive force fields [17] are state-of-the-art force fields that allow one to simulate complex chemical reactions. The key concepts that distinguish ReaxFF from the non-reactive force fields are the use of partial bond orders to describe covalent interactions as opposed to fixed connectivities in non-reactive force fields and the determination of charges by an extended charge equilibration scheme that includes both charge transfer and polarizability self-consistently and instantaneously. The bond order is determined by bond length and goes to zero when the bond is dissociated, such that bond length -> bond order -> bond energy. Polarizability is accounted for by allowing transfer between atoms of the variable valence or shell charge w.r.t. the fixed core charge through the use of self-consistent charge equilibration model. Other concepts used in ReaxFF are Morse potentials for non-bonded interactions (Van der Waals and Pauli repulsion) and over and under coordination corrections. These aspects make ReaxFF very attractive for modeling processes where bonds break and form such as traversing configuration space.

2.4. Tight Binding

For electronic structure calculations, tight binding provides a computationally less complex and highly scalable alternative to *ab intio* methods like GW. The basic philosophy of tight binding is bottom up modeling where the electronic system is considered not as a freely extending electron gas, but as a system built atom by atom. The wave function is therefore represented as a Bloch sum on a set of basis functions where the same basis functions sit on each lattice site (linear combination of atomic orbitals or LCAO). The Hamiltonian entries in the matrix representation carry parameters that are obtained empirically. Empirical nature makes this method less transferable than an *ab initio* method. However, use of empirical parameters to construct the Hamiltonian matrix, which is then diagonalized to obtain the eigenenergies, makes this is a fast and scalable method.

2.4.1. Slater-Koster formulae

When using tight binding, it is most convenient to define parameters such that they are minimized in number. The atom interaction parameters of the Hamiltonian are, therefore, referenced to the bond between the two atoms (for nearest neighbor tight binding). This allows the use of these same parameters for all atoms/ bonds that see the same environment (e.g. in diamond lattice) no matter how the bond is oriented. When constructing the Hamiltonian matrix, however, one has a universal set of axes, and so one needs a basis transformation (rotation of axes, using spherical harmonics) from the bond and orthogonal directions to the universal axes direction. Slater and Koster [18] provided these transformation formulae when they formulated tight binding.

2.4.2. $sp^3d^5s^*$ orthogonal parameters and corrections

Klimeck and colleagues [19, 20] carried out optimization of orthogonal (i.e. overlap matrix of basis functions is identity) $sp^3d^5s^*$ parameters using genetic algorithms to fit to band edges and effective masses to *ab initio* results at certain symmetry points of bulk material. Use of orthogonal parameters simplifies the eigenvalue problem to be dealt with by making the overlap matrix identity. Later, Boykin *et al.* [21] suggested modifications to the atom self entries of the Hamiltonian by introducing extra parameters to take into account strain in the system. This has increased the applicability and transferability of the bulk $sp^3d^5s^*$ parameters.

3. PREDICTING NANO-STRUCTURE

The first step in device invention and design is to obtain the appropriate material. For futuristic nano-devices, nano-structure prediction remains a significant problem, especially for small structures where surface atoms play such a dominant role that they can drive changes in the underlying crystal configuration. To predict the structure as well as mechanical and electronic properties of nanostructures one can, in principle, use *ab initio* electronic structure methods, such as density functional theory (DFT), which provide an accurate description of the interaction between atoms from first principles. However, these methods are computationally so intensive that they cannot be applied to cases where the ground state structure is not known and an extensive exploration of configuration space is required. Thus, most *ab initio* studies have so far been limited to the characterization of pre-determined structure designs based on intuition or the behavior of similar materials. A computationally less intensive alternative is offered by inter-atomic potentials or force fields (where atomic interactions are described via potential energy functions designed to reproduce the role of electronic structure). Together with molecular dynamics (MD) or Monte Carlo methods, force fields can be used to explore configuration space in search of the ground-state structure. However, despite recent breakthroughs, interatomic potentials remain less accurate and predictive than *ab initio* methods. To address this situation, a combination of MD and DFT calculations is proposed here to predict the structure of nanoscale materials and this methodology is applied to investigate stable sub-nanometer diameter Si nanowires.

3.1. Case study – sub-nanometer tubular silicon nanowires

3.1.1. Brief history of small diameter 1-D silicon nanostructures

Silicon nanowires have been around for more than a decade and fabricated by several research groups.[5, 22] These are mostly surface passivated with H or oxide. Diameter dependence of the orientation of the Si nanowire has also been investigated in the past, [5, 23] ([110] and [112] wires are more favorable as diameters become small). A

major excitement about small diameter Si nanowires came when Ma *et. al.* [22] successfully fabricated <2 nm diameter H passivated [110] and [112] Si NWs in the lab. These wires were reported to retain Si bulk geometry and had band gaps higher than 3 eV conforming with the general trend of confinement on bandgap. Unpassivated SiNW of larger diameters had also been successfully fabricated earlier by Marsen and Sattler. [24] They suggested non-bulk fullerene cores for these wires. Kagimura *et al.* [25] studied theoretically the diameter dependence of wire orientation and found that below 1.1 nm diameter, the bulk like geometries are not the most stable configurations for both Si and Ge nanowires. For Si NW they suggested simple hexagonal wire geometry to be the most stable for sub-nanometer diameters. In 2005, Bai *et al.* [26] showed that metastable pentagonal and hexagonal cross-section hollow silicon nanowires (silicon nanotubes) were metallic. Ponomoreva *et al.* [27] have simulated a Si-34 cathrate nanotube structure and reported its transport properties. Thus, one finds that though, owing to the promise offered by Si 1-D structures in various areas of application ranging from electronics to biological detection, research in this area abounds, there is no clear picture of the relative stability of the various proposed sub-nanometer structures. Moreover, the structures so far are all intuitive or derived from other atomic level structures of silicon. This work [28] shall endeavor to predict new atomic level structures of sub-nanometer silicon nanotubes and compare the energetics of sub-nanometer silicon nanowires.

3.1.2. Questions to be answered

This work (this and next chapter) endeavors to answer the following questions:

• Can we predict these 1-D nanostructures as opposed to making intelligent guesses?

• How does surface affect configuration of small diameter 1D silicon nanostructures?

• How do silicon nanotube (hollow) structures compare with other nanowires at close to one nm diameters?

• (In chapter 4) What are the properties of these tubes? Should the experimentalists try making them in the lab?

3.2. Approach

(See figure 3.1) The approach here to predict the structure of nanoscale materials consists of two steps: i) starting from a simple trial structure, MD with an accurate force field is used to carry out an annealing procedure, which explores configuration space and leads to well relaxed structures, ii) the most promising structures obtained from the MD simulations are fully relaxed using energy minimization with DFT within the generalized gradient approximation (GGA). Thus, the strategy described here combines a computationally less intensive approach to explore configuration space with a more accurate and computationally intensive method to refine the results. It must be emphasized that this is a generally applicable approach that can be used with any material for which an accurate force field exists. The force field should be able to capture how environment affects bonding and describe configurations very different from the bulk ground state; this is critical since the DFT minimization (step ii) will lead to the local minimum directly downhill from the initial configuration. Significant progress has occurred recently in this area and descriptions for a wide range of materials exist today, see for example Refs. [17, 29, 30]. The remainder of the chapter applies this procedure to predict the structural properties of the tubular Si NWs (Si NTs).
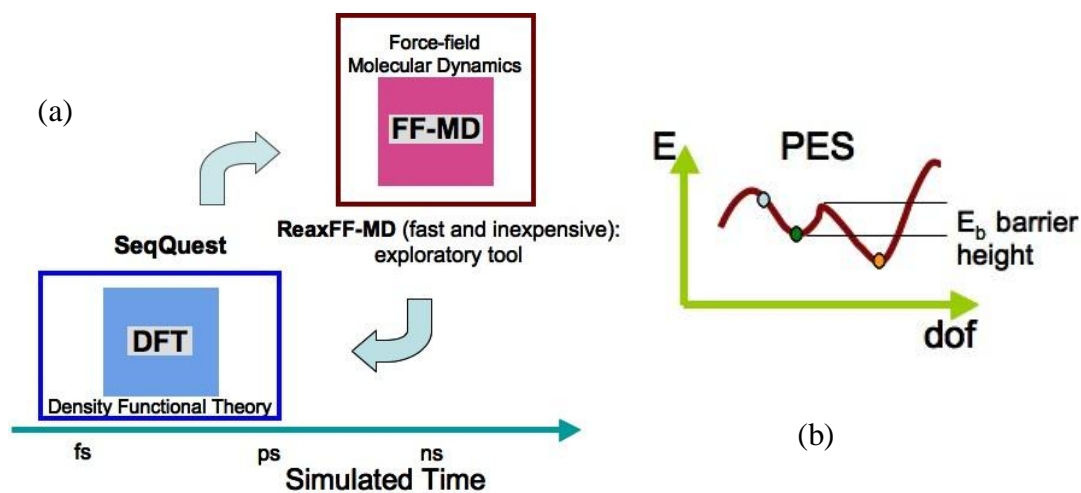
Fig. 3.1 (a) The simulation approach applied in this work. (b) The potential energy surface showing the local and global minimum. A structure at the configuration shown by light blue point can get trapped in a local minimum (green point) and needs external force during dynamics to be pushed into the global minimum (orange point)

3.2.1. Step 1: Molecular Dynamics

Pentagonal and hexagonal NTs (rows of atoms arranged in pentagons or hexagons) are used since they are the simplest metastable tubular structures.[26] Different trial geometries with 5, 6, 10, 11 and 12 rows of pentagons or hexagons allow for
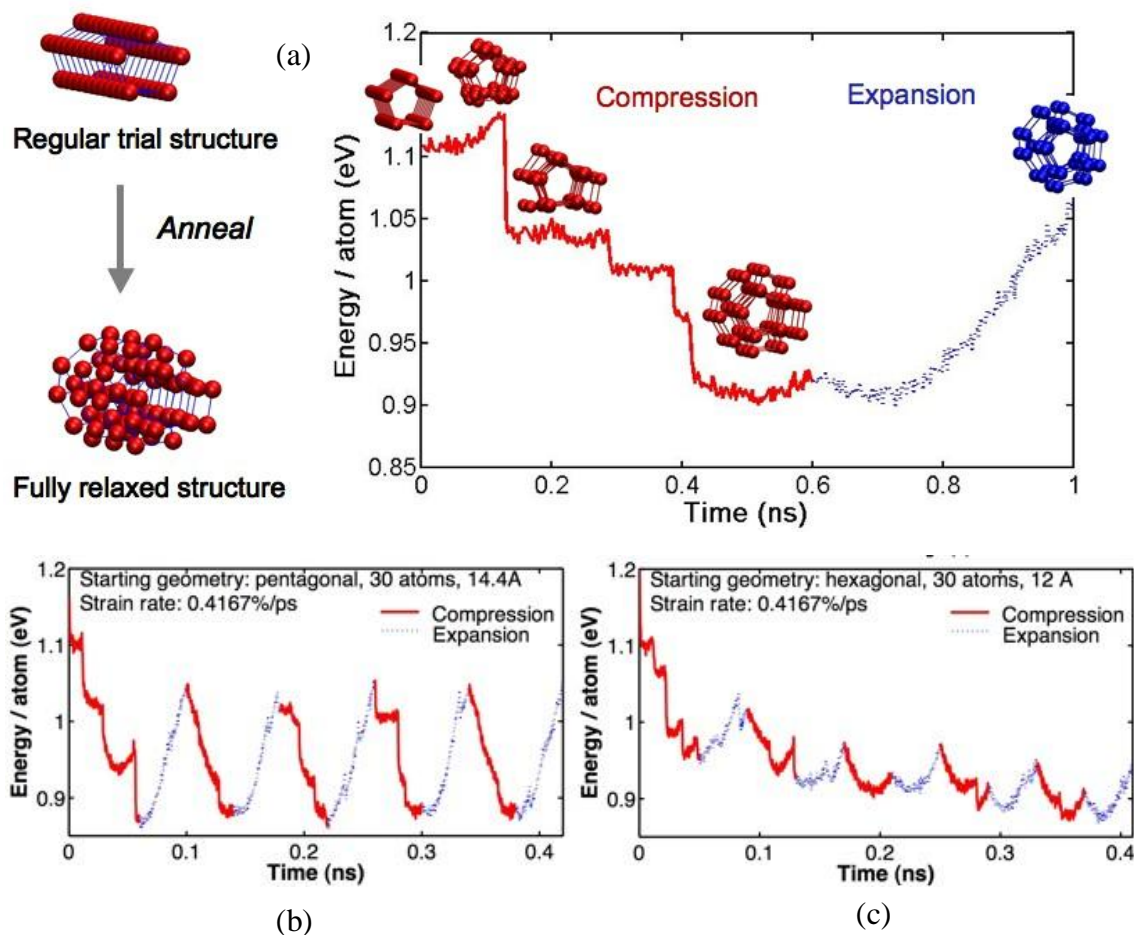
Fig. 3.2 (a) The relaxation process during ReaxFF-MD of the trial structures. Shown is a single expansion and compression cycle for a 30 atom unit cell pentagonal tube. The solid curves represent compression and the dotted part represents expansion of the tube. (b)-(c) Energy as a function of time during cyclic loading of an initially (b) pentagonal tube of 30 atoms strained by 0.06 A/ps using MD with ReaxFF at T=300 K and (c) hexagonal tube of 30 atoms strained by 0.05 A/ps using MD with ReaxFF at T=300 K.

different possible periodicities of the final structure. To obtain well relaxed NTs (see fig. 3.2(a)), the trial structures are cyclically compressed and expanded using MD at two temperatures (300 K and 600 K) with ReaxFF, a reactive potential that has been shown to accurately describe atomic interactions in Si, including the process of crack

propagation.[31] For each initial configuration and temperature, various cyclic mechanical loadings: three ranges of strain (-37.50% <ε< -12.50%, -25.00% <ε< -8.30%, -20.87% <ε< -4.17%) and three strain rates (0.04167 %/ps, 0.41667 %/ps, 0.83333 %/ps) are applied. This makes thermal and mechanical energy available to the system to overcome energy barriers that may separate the initial trial structure from lower-energy configurations and allows the NT to find its natural length. Figure 1 shows the potential energy as a function of time for two MD annealing simulations corresponding to pentagonal [Fig. 3.2(b)] and hexagonal [Fig. 3.2(c)] initial structures at T=300 K and strain rate of 0.4167 %/ ps. Both cases show abrupt energy drops that correspond to configurational changes and rather well behaved energy-length relationships between structural transitions. In some simulations, the lowest energy configuration is attained in the first compression-expansion cycle, see Fig. 3.2(b), and subsequent mechanical cycles do not result in additional relaxation. In other cases, exemplified in Fig. 3.2(c), several cycles are required before a periodic behavior is achieved. In view of the various strain rates and ranges, MD simulations with timescales ranging from 0.2 to 2.7 nanoseconds are performed. (Note that this is well beyond what is possible today with *ab-initio* MD.) An analysis of the structures resulting from the MD annealing procedure leads to the following general observations: i) the longer initial structures (consisting of 11 and 12 rows of atoms along the tube axis) buckle and consequently do not lead to one-dimensional structures for the high strain rates accessible to MD; ii) about 15% of the simulations starting from 5, 6 or 10 row structures lead to hollow 1-D tubes; iii) pentagonal trial structures lead to a larger percent of nanotubes as compared to hexagonal ones.

3.2.2. Step 2: Density Functional Theory

The eight most promising configurations from the MD simulations were relaxed and length optimized (fig. 3.3) using DFT within the GGA approximation [32] with the code SeqQuest.[33] SeqQuest uses local orbital basis sets of atom- and potential-dependent contracted Gaussian functions, and non-local, norm-conserving Hamman pseudo-potential developed for the GGA functional. 4.9 spatial grid points per bohr, temperature of occupation ~158 K and maximum force limit of 0.0002 ryd/bohr for geometry optimization were used.

DFT relaxation of the MD structures led to low-symmetry tubular structures with similar energetics (within a range of 0.05 eV/ atom with some structures separated by less

than 0.026 eV/ atom); the 8 structures converged into three topologically distinct NTs during minimization.
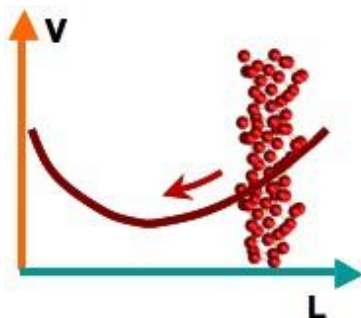
Fig. 3.3 Relaxation and length optimization of the ReaxFF relaxed structure using DFT-GGA

3.3. Tubular structures of very small diameter clean silicon nanowires

Figure 3.4 shows the atomic structure of the lowest-energy tubular structures known to date. The disordered nanotube (DNT) structures resulting from our MD-DFT approach are denoted DNT1, DNT2 and DNT3; these were obtained from 30-atom pentagonal, 30- atom hexagonal and 25-atom pentagonal trial structures respectively. Together with the DNTs we show fullerene-based structures that reduce their symmetry during DFT energy minimization; these distorted fullerene structures are denoted DF1 and DF2. Table 3.1 summarizes various properties of these structures as well as others proposed earlier (energies reported in Table 3.1 and in the remainder of this paper are given per atom and with respect to the diamond structure). Various low-energy tubular structures with similar stability are obtained; these structures are either DNTs obtained from the described MD-DFT procedure or are fullerene-like. Structures F1 and F2 in Table 3.1 are fullerene-based and were proposed earlier;[24] if their full symmetry (discussed later) is not enforced during relaxation they transform into DF1 and DF2, DF2' or DF2'' with lower symmetry and energy. Ponomareva and collaborators [27] have reported DF2'' as Si-34 clathrate structure. It is interesting to note that structure DF2' is a defective but energetically similar form of DF2'' while DNT2, resulting from our annealing procedure, is a defective form of fullerene structure DF2 with higher energy than its parent structure. Table 3.1 also shows that the pentagonal and hexagonal trial structures (denoted Pen and Hex) are highly strained, high-energy structures and so are carbon nanotube-based structures. We find an energy of 0.805 eV for the armchair (4,4)
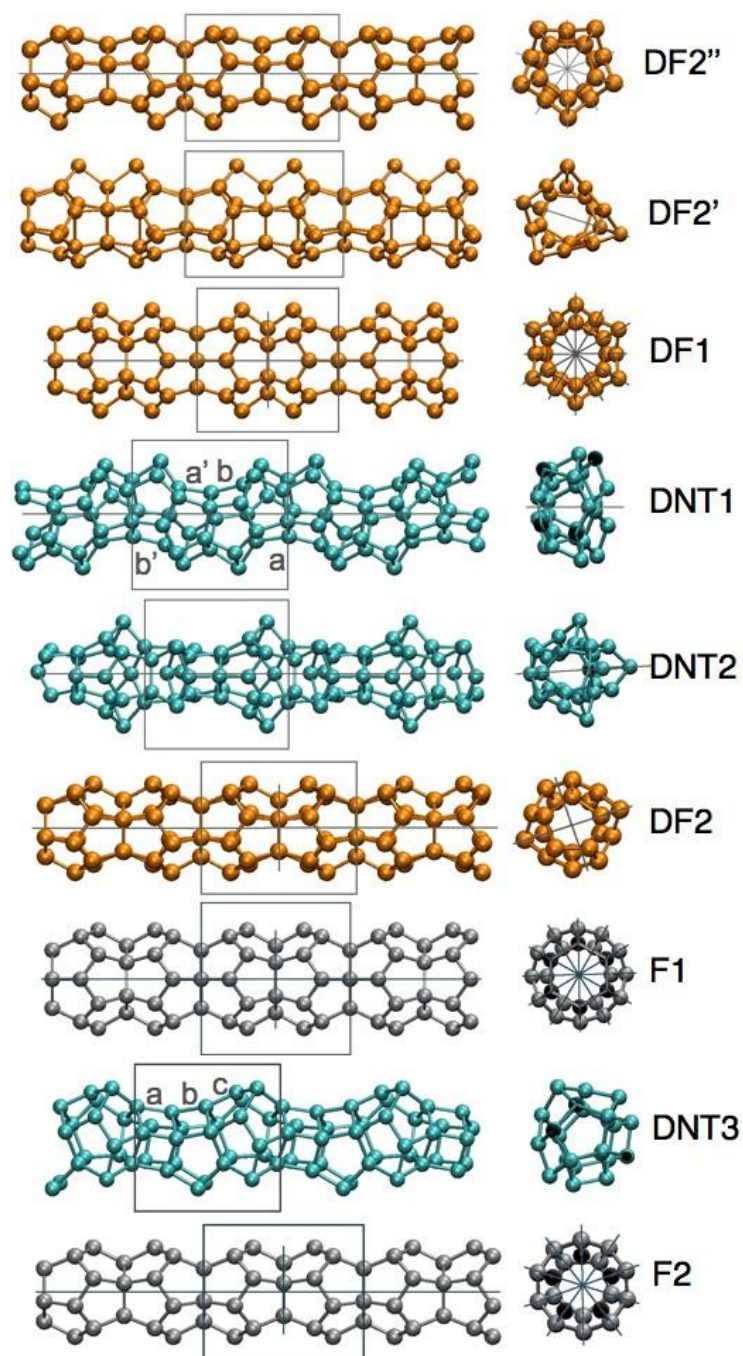
Fig. 3.4 The sub nanometer diameter tubular clean silicon nanowire structures, arranged in order of decreasing cohesive energies (from top to bottom). The solid boxez in the longitudinal view mark the unit cell boundaries. The lines in the longitudinal and cross-sectional views represent the different axes and planes of symmetry described in the text.

CNT structure (Zhang *et al.* [34] found armchair configurations to be more favorable than

zigzag (m,0) structures). Here it is concluded that the low energy unpassivated sub-nanometer silicon nanotubes (hollow nanowires) are energetically more favorable than the unpassivated nanowires of similar dimensions.

TABLE 3.1 DFT-GGA properties of silicon nanostructures. DNT1, DNT2 and DNT3 are disordered structures obtained from our annealing procedure; DF1 and DF2 are distorted fullerene structures and F1 and F2 are the corresponding parent structures. Simple pentagonal (Pen) hexagonal (Hex) and carbon nanotube (CNT) structures are also shown. We also show two simple-hexagonal wires with different radii; these non-hollow structures are denoted SHW1 and SHW2. For each structure, we report its periodic length (L), number of Si atoms in its unit cell (n_{Si}), cross-sectional area (A), energy (per atom and with respect to diamond structure) obtained from SeqQuest (ε_S), Young's modulus (E, from SeqQuest) and energy obtained from ABINIT [35, 36] (ε_A). Bold indicates structures reported here for the first time (as explained in the text, DF1 and DF2 are topologically equivalent to F1 and F2 but have lower symmetry).

Structure	L (Å)	n_{Si}	A (Å^2)	ε_S (eV)	ε_A (eV)
DF2''	**10.70**	**30**	**-**	**0.636**	**0.601**
DF2'	**10.70**	**30**	**74.9**	**0.637**	**0.602**
DF1	**10.64**	**36**	**80.9**	**0.638**	**0.604**
DNT1	**11.12**	**30**	**81.8**	**0.658**	**0.615**
DNT2	**10.58**	**30**	**86.0**	**0.673**	**0.625**
DF2	**10.93**	**30**	**67.6**	**0.697**	**0.668**
F1	10.86	36	72.2	0.705	0.629
DNT3	**9.79**	**25**	**69.4**	**0.708**	**0.653**
F2	10.97	30	57.9	0.714	0.689
Pen	2.42	5	33.3	0.755	0.724
Hex	2.40	6	40.7	0.774	0.744
CNT (4,4)	3.89	16	324.7	0.805	-
SHW1	2.49	13	90.2	0.663	0.702
SHW2	2.64	7	40.7	0.751	0.822

The fullerene-based structures F1 and F2 have 6- and 5-fold rotational symmetry around the tube axis respectively. The other rotational axes (two-fold) and reflection

planes are shown by lines in the cross-sectional view of the structures in Fig. 3.4. The symmetry operations for F1 are $\{(E/t),(C_{12}|t/2),D_{6h}\}$ and for F2 they are $\{(E/t),(C_{10}|t/2),D_{5h}\}$. E is the identity operation, t represents the translational periodicity of the simulation cell along its axis, $(C_{12}|t/2)$ and $(C_{10}|t/2)$ represent screw symmetry operations; finally D_{6h} and D_{5h} are the Schönflies representation of the point group symmetries. Structure DF2 exhibits a considerable loss of symmetry compared to its parent structure F2 with only $\{(E/t),(C_2|t/2),(\sigma_v|t/2),D_{1h},\sigma_v'\}$ allowed; $(\sigma_v|t/2)$ denotes glide-reflection on a vertical plane containing the principal axis and σ_v' represents reflection through another vertical plane. It turns out the distorted fullerene DF2 structure is not the ground state of that structure. Further relaxation leads to additional symmetry breaking; the ground state structure, denoted DF2' retains symmetry operations $\{(E/t),D_{1h}\}$. Similarly DF1, $\{(E/t),D_{6h}\}$, has lower symmetry than F1 and DF2'', $\{(E/t),D_{5h}\}$, has lower symmetry than F2. It The MD annealing procedure substantially reduces both the translational and rotational symmetries of the initial trial structures and the resulting DNT structures have less symmetry than fullerene-based ones. The translational symmetry of all DNTs along their axes is reduced to the minimum allowed by the periodic boundary conditions. All DNTs can be described as a chain of atomic cages interconnected by five- or six-membered rings. DNT1 consists of four cages, denoted a, b, a', b' within its unit cell, see Fig. 3.4. The cages are connected by 5-atom ring cross-sections. Cages a' and b' are reflections of cages a and b respectively through a plane σ_v, parallel to the longitudinal axis of the tube and marked by lines in the two views of the structure in Fig. 3.4. The space symmetry operations of DNT1 are $\{\{E/t\},(\sigma_v|t/2)\}$. Structure DNT2 is a defective form of the 30-atom-unit-cell fullerene structure DF2 in which an atom from one of the two cages moves into the other one causing significant geometrical distortions. The symmetry operations of DNT2 are $\{(E/t),C_{1v}\}$ (the mirror plane is shown in Fig. 3.4). Finally, the only symmetry operation remaining in DNT3 is (E/t). The structure can be described by three cages a, b and c, see fig. 3.5, interconnected by 5-membered atomic rings. We found two enantiomers of this structure when performing MD simulations. One was found when straining the 25 atom pentagonal structure within -37.50% $<\varepsilon<$ -12.50% with $\varepsilon=$ 0.04167% /ps and the other when straining it within -25.00% $<\varepsilon<$ -8.30% at ten times the rate. This indicates that our approach is robust and the resulting structures can be generated by various pathways. It is also to be observed that DF2' and DF2'', which are the most stable unpassivated structures, have a difference in energies smaller than kT at room temperature. Thermal energy may therefore lead to a dynamical coexistence between the two structures.

Additional insight into the various structures can be gained from radial distribution functions (RDFs), shown in Fig. 3.5(a), and the distribution of coordination numbers (number of nearest neighbors), shown in Fig. 3.5(b). Fullerene based structures exhibit a split first RDF peak that originates from atoms having 3 or 4 nearest neighbors leading to

(a)

(b)

(c)
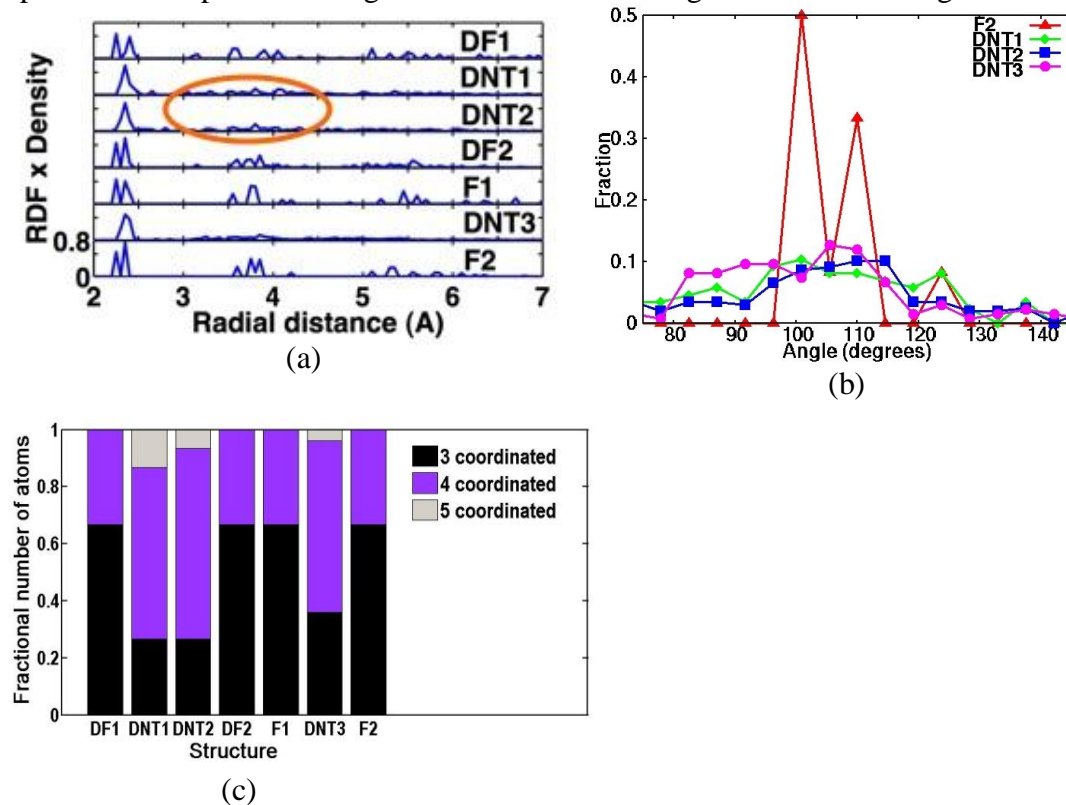
Fig. 3.5 (a) The atomic density times radial distribution function plot for various Si nanotube structures, obtained at a resolution of 0.05 Å. (b) Bond angle distribution for a fullerene SiNT (F2) and the three disordered nano-tubes (DNTs). (c) Histogram showing the fractional number of 3, 4 and 5 coordinated atoms in the nanotube structures.

three types of bonds in order of increasing length: i) between two 3-coordinated atoms, ii) between a 3-coordinated and a 4-coordinated atom and, iii) between two atoms with 4 nearest neighbors. [Only two peaks are seen in Fig. 3.5(a) due to the resolution of the RDF calculation.] On the other hand, the disordered nanotube structures exhibit a single first peak since the atomic bonding environment cannot be grouped into two well-defined categories. A second difference in the RDFs is that the second peak for the DNTs is significantly more diffuse than that for the fullerene ones. Angle distribution functions (fig. 3.5(b)) of the DNTs are also significantly more diffuse than for fullerene nanotubes, a further indication of the disorder of the structures. In order to define first nearest

neighbors needed to calculate coordination number information shown in Fig. 3.5(c) we use a cutoff distance of 2.70 Å (15% larger than the Si-Si bond distance in diamond). Figure 3.5(c) shows that fullerene structures have twice as many 3 bonded atoms as 4-bonded ones. This ratio gets modified in favor of the higher coordination for the distorted nanotube structures. They contain a higher proportion of 4-coordinated atoms than 3-coordinated ones; furthermore, the histograms also show some 5-coordinated atoms. This last number is very sensitive to the choice of cutoff as is commonly found in disordered structures and apparent from the RDF plots. For instance, if the cut-off is reduced to 2.50 Å, no "5-bonded" atoms are found.

3.4. Structures of very small diameter hydrogen passivated silicon nanowires

All the structures described in 3.3 are passivated by adding an H atom to each dangling bond on the surface Si atoms of each nanostructure (figure 3.6). These structures are then fully relaxed via energy minimization with respect to all atomic positions and simulation cell dimensions using DFT-GGA. The bulk-like wires shown in Fig. 3.6(d) were surface reconstructed by carrying out ReaxFF MD at 300K before hydrogen passivation and DFT relaxation.
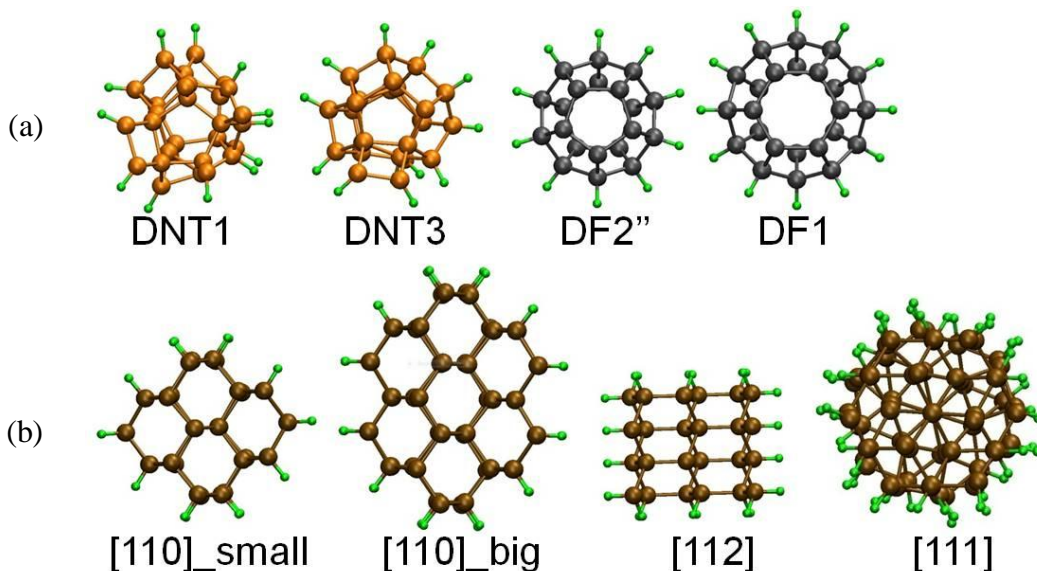
Fig. 3.6 (a) Relaxed hydrogen-passivated DF and DNT structures; upon passivation the DF structures undergo a transformation to undistorted fullerene core, (b) H-passivated diamond-core wire structures simulated for comparison.

Upon passivation, the DF nanotube structures relax to the symmetric, perfect-fullerene structures, see Fig. 3.6. This is equivalent to what happens on asymmetrically reconstructed Si(100) surface when passivated with one H atom per surface Si atom. As seen in Fig. 3.6, the more disordered DNT structures do not undergo such drastic structural evolution when H passivated.

To calculate the formation energies of the H-passivated nanowires, two different reference systems are used:

i) Formation of silane from atomic silicon:

$$\varepsilon_{SiNT/SiAtom} = \left[\frac{E_{SiNT} - n_H \left(\dfrac{E_{Silane} - E_{SiAtom}}{4} \right)}{n_{Si}} \right] - E_{SiBulk} \qquad (3.1)$$

where $\varepsilon_{SiNT/SiAtom}$ is the total formation energy of the SiNT, E_{SiNT} is the total energy of the nanotube, E_{SiH_4} is the ground state energy of an isolated silane molecule, E_{SiAtom} is the energy of an isolated Si atom, E_{SiBulk} is the ground state energy per atom in diamond Si and n_H and n_{Si} are the number of H and Si atoms, respectively, in the SiNT.

ii) Formation of monohydride on Si(100) surface:

$$\varepsilon_{SiNT/Si(100)Surf} = \left[\frac{E_{SiNT} - n_H \left(\dfrac{E_{Si(100)HSurf} - E_{Si(100)cleanSurf}}{2} \right)}{n_{Si}} \right] - E_{SiBulk} \qquad (3.2)$$

$\varepsilon_{SiNT/Si(100)Surf}$ is the total formation energy of the SiNT, $E_{Si(100)HSurf}$ is the ground state energy per dimer of a Si slab with (100) surface and $E_{Si(100)HSurf}$ is the ground state energy per dimer of a Si slab with (100) surface.

TABLE 3.2 Table listing the atomic population (n_{Si} and n_H), unit lengths L, the cross-sectional areas A (see text for calculation method), energies ε per silicon atom [calculated using equation (3.2)] of the ~1nm diameter hydrogen passivated 1-D silicon nanostructures shown in figure 3.7

Structure	n_{Si}	n_H	L (Å)	A (Å^2)	ε (eV)
DNT1	30	12	11.10	129.27	0.788
DNT3	25	12	9.90	118.48	0.870

F2	30	20	10.50	111.24	0.827
F1	36	24	10.20	130.32	0.829
110_small	32	20	7.60	166.62	0.734
110_big	48	24	7.60	222.44	0.593
111	76	48	18.93	155.89	0.792
112	48	40	13.40	154.40	0.948
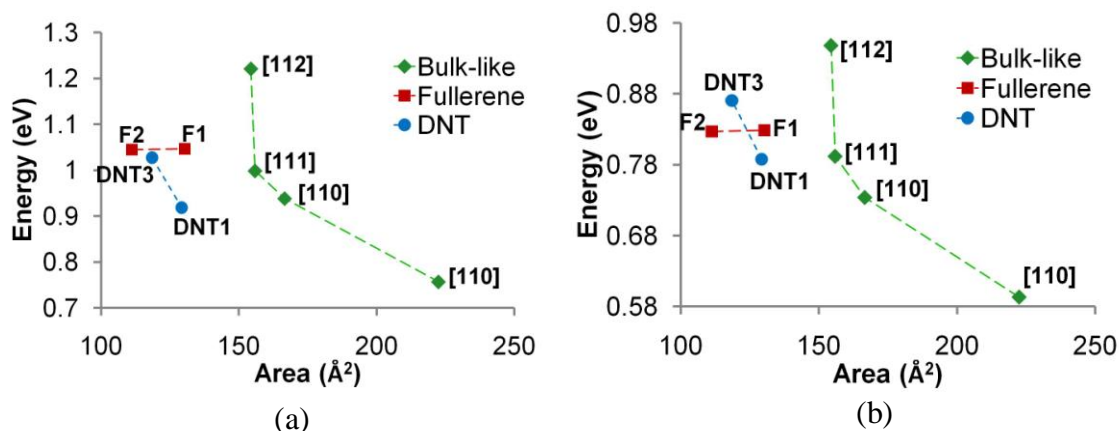
Fig. 3.7 Plot of formation energy calculated using (a) equation (3.1) and (b) equation (3.2) versus the cross-sectional area of H passivated nanowires

Equations (3.1) and (3.2) provide the total cohesive energy of the SiNTs. Table 3.2 summarizes the formation energies of the H-passivated SiNTs. Since the energies of pristine wires are known to increase with decreasing diameter, the results for the H passivated wires are summarized in fig. 3.7(a) and (b) as plots of energy versus cross-sectional area. It should be noted that using either reference, considering their smaller cross-sectional size, the H passivated DNTs and Fs are at least energetically comparable to, if not better than, the passivated [110], [111] and [112] bulk wires. It should be noted that experimentalists have succeeded in fabricating wires of <2 nm diameter [22] which are believed to possess [110] and [112] diamond-like cores. The results reported here then indicate that the fabrication of DNTs and DFs is, from cohesive energy considerations, possible.

3.5. Conclusions

1.   For very small diameters (~<1 nm), non-diamond based tubular structures of silicon nanowires are energetically most stable. Several new such silicon nanowires

(distorted nanotubes or DNTs) are predicted using reactive force field molecular dynamics and density functional theory. These are energetically comparable to the low energy distorted fullerene nanotube structures(DFs). DF2' and DF2'' are the best among all clean nanowires.

2.   The distorted fullerene tubes have reduced symmetry and bond environements drastically different from silicon bulk. The distorted nanotubes carry, in addition, high disorder.

3.   The hydrogen passivated DNTs and DFs are at least comparable to, if not better than, the diamond-core nanowires at such diameters.

4. ELECTRICAL AND MECHANICAL RESPONSE OF NANO-MATERIALS

The last chapter showed that unpassivated sub-nanometer tubular Si nanowires - the distorted fullerenes and the distorted nanotubes obtained from MD and DFT - are theoretically the most stable unpassivated and passivated 1D silicon nanostructures known. It was however not discussed why one would want to go to such small diameters. Some recent theoretical studies have shown the benefit of using small diameter silicon nanowires in applications such as nano-mechanics[35] and thermoelectrics.[36] Such benefits arise from the properties of the nanowires. For example, small diameters are preferable for thermoelectrics because they show an increase in the power factor[36] and a decrease in both the electronic[36] and phononic[37] contributions to thermal conductivity. However, these studies assume bulk-like geometries for the wires. In this regard, this chapter asks the question: What are some basic properties of the stable structures predicted in the last chapter? The purpose is to inform experimentalists of the expected properties of the nanowires, so that an intelligent decision about endeavoring to fabricate these in the lab can be made based on the level of incentive in the effort. Here only density functional theory is applied for all investigations.

4.1 Case study – silicon nanotubes

4.1.1 Bandstructure of 1-D Si nanostructures in literature

Both theoretically [38] and experimentally,[22] researchers have found that bulk-like H passivated [110] and [112] Si nanowires have each a well-defined bandgap that increases as the wire diameter decreases, such that this gap is about 3.1eV for ~1 nm [110] wire and about 3.5 eV for ~1 nm [112] wire (see figure 4.1). On the other hand, when the surfaces are unpassivated and reconstructed, even 3.7 nm diameter [110] hexagonal cross section wires are found to be metallic from density functional theory within generalized gradient approximation (DFT-GGA) calculations.[39] However, the bandgap is shape dependent and for a rectangular [110] wire (which is highly distorted due

to surface reconstruction) the bandgap from DFT-GGA is about 0.35eV for a wire of effective diameter ~1 nm.[40] (It must be noted that at this diameter, hexagonal wires are energetically more favorable than the [110] wire.[25]) As the diameters become smaller than 1 nm, unpassivated hollow wires (nanotubes) of regular cross-sectional configurations (square, pentagonal or hexagonal), proposed by Bai et. al,[26] are found to be metallic using DFT calculations. From PM3 calculations, Marsen and Sattler report bandgaps ranging between 0.5 to 1.5 eV for <1nm diameter F1 and F2 clusters.[24]
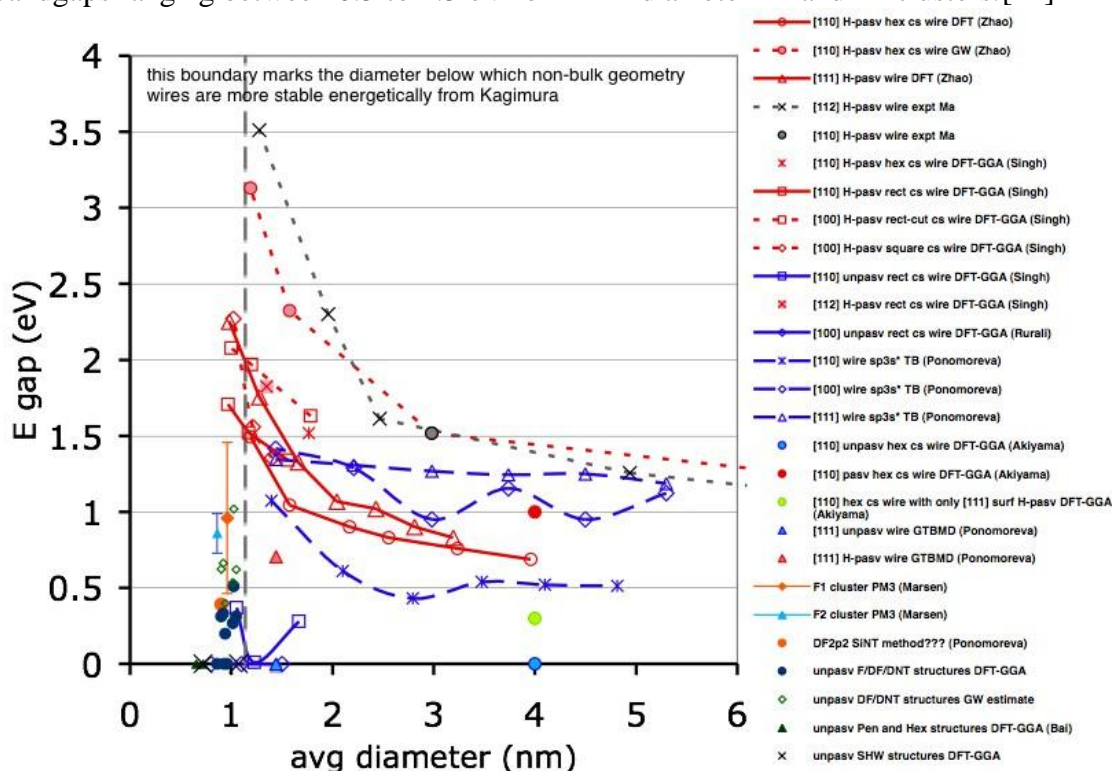
Fig. 4.1 The bandgaps versus diameter for the various 1-D Si nanostructures studied in literature. The unpassivated, reconstructed wires are shown in blue and the H passivated wires are shown in red. The empty and filled green circles represent bandgaps from this work for unpassivated SiNTs.

This chapter reports that the energetically better silicon nanotube structures (hollow silicon nanowires) are unambiguously semiconducting unpassivated 1-D Si nanostructures of diameter <1 nm. The disordered nanotube DNT3 has the highest bandgap of all these sub-nanometer unpassivated Si nanostructures, and that this bandgap is about three times smaller than the bandgaps of bulk-like H-passivated nanowires of similar sizes. It is also shown that the semiconducting nature of these nanotubes can, at a more fundamental level, be coupled with the symmetry and disorder of the tubes. The

band structures of these materials when they are H passivated are also investigated. It is observed that while H passivation leads to an increase in the bandgap for all, passivation affects the bandgaps of DFs and DNTs to different degrees.

4.2 Electronic bandstructure of small diameter silicon nanowires from DFT

All DFT calculations presented here were performed within the generalized gradient approximation of Perdew-Burke-Ernzerhof (GGA) using the plane-wave basis code, ABINIT.[41, 42] The SCF calculations here employ 2 k points along the periodic direction. For the plane-wave basis in ABINIT, a cutoff energy of 12 Hartree was used. The potential was Pulay mixed with 7 previous iterations during SCF iterations. A tolerance of 0.027 μeV was set on the absolute difference of total energies which, when reached, causes an SCF cycle to stop. The ionic configuration was relaxed using the Broyden-Fletcher-Goldfarb-Shanno minimization to reduce the internal forces to less than 2.57 eV/Å.

It should be noted that, as frequently done in literature, this thesis reports the K-S eigenvalues and associated eigenfunctions obtained from DFT. For semiconductors like silicon, the K-S bandgap is often smaller than the experimental one. While a more accurate description of the bandstructure could be obtained by carrying out many-electron perturbation (GW) corrections on the DFT bandstructure, the focus of the chapter is on trends obtained from the K-S eigenvalues.

4.2.1 DFT bandstructures of unpassivated nanowire/ tube structures

The K-S bandstructures from DFT-GGA of the various unpassivated wires are shown in Fig. 4.2 and the key features are summarized in Table 4.1. Here bandgap is defined as the difference between the energy E_{LUMO} of the lowest unoccupied molecular orbital (LUMO) and the energy E_{HOMO} of the highest occupied molecular orbital (HOMO). The results show that while the high-symmetry (and unstable) perfect fullerene NTs have zero bandgap, their structural relaxation to DFs opens a band gap. All relaxed DNT structures are also semiconducting. All DFs and DNT1 possess direct band-gaps while DNT2 and DNT3 are indirect band gap semiconductors. As noted earlier, the K-S bandgap is typically smaller than the true bandgap. Experimental results for bulk Si and H passivated silicon nanowires and GW calculations, that incorporate corrections to K-S energies from many-body perturbation theory, for unpassivated Si (100) surfaceshow that

the Kohn-Sham bandgap is between 1.6 and 2.6 times smaller than E_{LUMO}-E_{HOMO}. Using a multiplicative factor of 2, we estimate the bandgaps of the unpassivated SiNTs to lie in the range 0.4-1.0 eV.
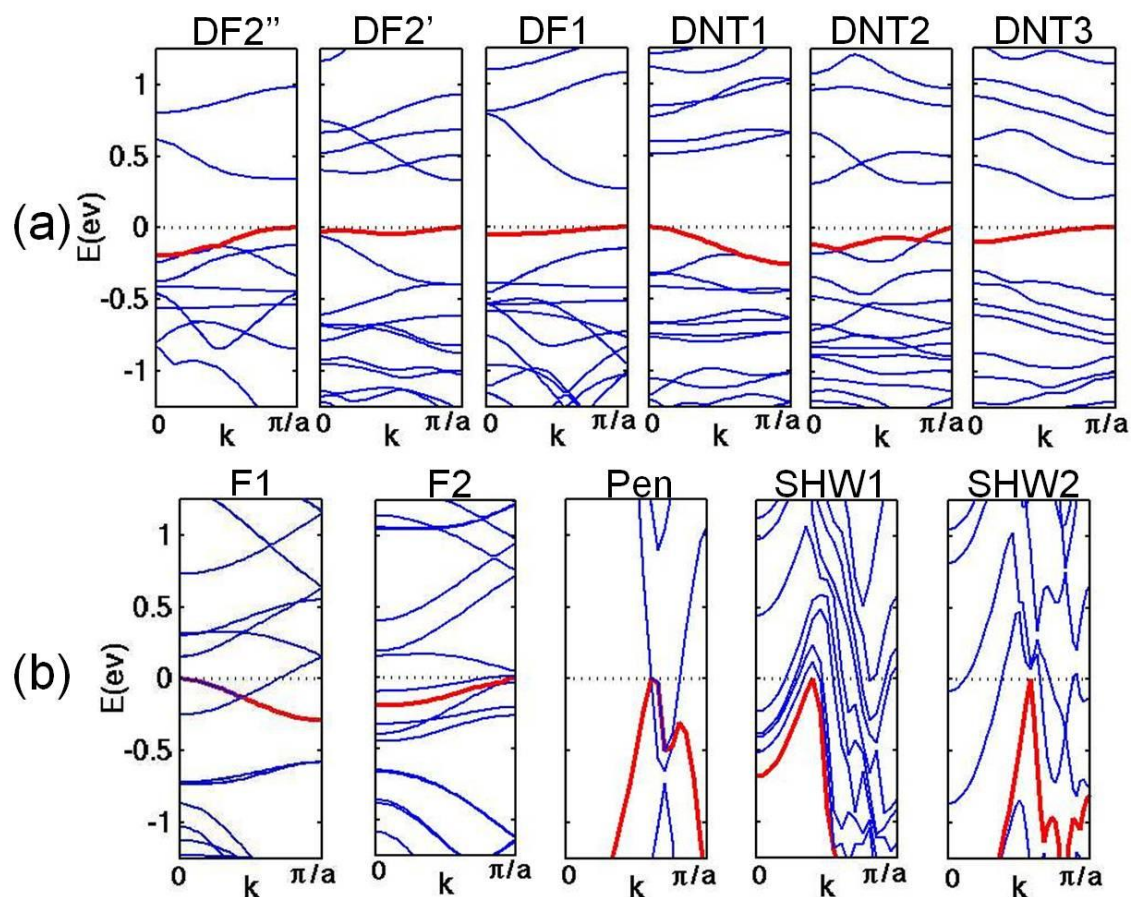
Fig. 4.2 (a) The calculated DFT band-structures of unpassivated nanowire structures of small diameters with the HOMO at 0eV (the top filled band at 0K is shown in bold red and the dotted line represents the zero energy axis) of (a) the low symmetry structures, DFs and DNTs from MD and DFT, (b) the more symmetrical structures including Pen and SHW1-2

The semiconducting nature of all DFs and DNTs reported here is in contrast with most previous reports on small diameter, clean, one-dimensional Si structures where metallic behavior was observed. Zero band gaps were predicted using DFT for regular pentagonal and hexagonal tubes, hexagonal and rectangular [110] nanowires of 4 nm and 1.2 nm diameters respectively, and using tight binding molecular dynamics calculations for [111]-oriented wires of diameter 1.44 nm. The only report of semiconducting behavior for this regime that the author is aware of is for some [110] rectangular wires of diameters between 1 and 2 nm although the same calculations predict zero bandgaps for other similar

cases. In contrast, the results reported here show unambiguously that *all* fully relaxed sub-nanometer SiNTs are semiconducting.

Table 4.1 also shows that the DFs and DNTs have, in general, high carrier effective masses, which are calculated considering all significant states close to HOMO and LUMO, and tend to strongly favor transport of one carrier, either hole or electron. The possible causes of such high effective masses include the hollow structure of the wires and the modified bond environments. This is supported here by the observation that the structural difference of energetically similar DF2' and DF2'' makes their effective masses strikingly dissimilar. Also, elsewhere in literature, defects on nanowire surfaces have been shown to affect the form and curvatures of the bands, especially those near the gap.

TABLE 4.1 Table listing the unit cell length (a), number (n_{Si}) of Si atoms in unit cell, energies per atom above Si bulk calculated in ABINIT (ε), the band energy gap ($E_g = E_{LUMO} - E_{HOMO}$ if positive) and the direct (D) or indirect (I) nature of the gap, all obtained from DFT-GGA, for the best silicon nanotube and nanowire structures of diameter ~1nm. The last two columns report the curvature electron effective mass m_e* (at LUMO) and hole electron mass m_h* (at HOMO) referenced to the free electron rest mass m_0.

Structure	a (Å)	n_{Si}	ε (eV)	K-S E_g from DFT-GGA (eV)	D/I	m_e*/m_0	m_h*/m_0
DF2''	**10.73**	**30**	**0.601**	**0.340**	**D**	**1.38**	**0.86**
DF2'	**10.76**	**30**	**0.602**	**0.331**	**D**	**0.52**	**2.10**
DF1	**10.63**	**36**	**0.604**	**0.268**	**D**	**0.65**	**4.75**
DNT1	**11.10**	**30**	**0.615**	**0.510**	**D**	**1.64**	**0.49**
DNT2	**10.47**	**30**	**0.625**	**0.311**	**I**	**0.58**	**0.26**
F1	10.86	36	0.629	0	-	-	-
DNT3	**9.90**	**25**	**0.653**	**0.199**	**I**	**0.15**	**0.67**
DF2	10.93	30	0.668	0	-	-	-
F2	10.97	30	0.689	0	-	-	-
Pen	2.42	5	0.724	0	-	-	-
Hex	2.40	6	0.744	0	-	-	-
SHW1	2.45	13	0.702	0	-	-	-
SHW2	2.4	7	0.822	0	-	-	-

4.2.2 Stability, bandgap and symmetry of unpassivated structures

Figure 4.3 shows that a correlation exists between the cohesive energy of the NT and the K-S band gap within each structural group (DFs and DNTs). In each individual category, the band gap increases as the stability of the tube increases. The more disordered DNTs exhibit, in general, higher bandgaps than the DFs of similar cohesive energies.
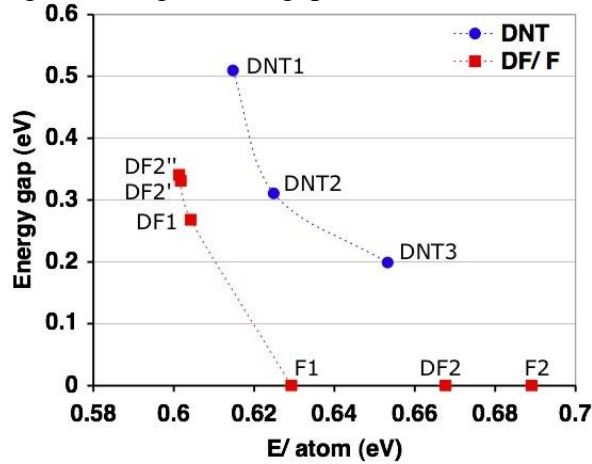
Fig. 4.3 The DFT energy gap versus energy/ atom measured with respect to Si bulk for the lowest energy unpassivated structures

To understand the reasons why a bandgap opens when the perfect fullerene structures relax into lower symmetry structures (DF families) we compare the topologies of their Kohn-Sham HOMO and LUMO orbitals for the F1 and DF1 pair. The band-structure of F1 shows the following degeneracies: E_{HOMO} (k=0) = E_{LUMO} (k=0) and E_{HOMO} (k=π/a) = E_{HOMO-} (k=π/a). Here a is the lattice constant and HOMO- represents the orbital right below the HOMO band. Figures 4.4(a), (b) and (c) show the F1 wavefunction isosurfaces [$|\psi|$=5 bohr$^{-3/2}$] corresponding the LUMO, HOMO and HOMO- orbitals for k=0 and k=π/a. Though orthogonal ($< \psi_{LUMO}(k=0) | \psi_{HOMO}(k=0) > = 0$) the LUMO and HOMO wavefunctions are related such that one can be obtained from the other merely by a screw motion (translation of a /2 and rotation of 30°). But for DF1 (Fig. 4.4(d) and (e)), the reduction in the symmetry of the structure modifies $\psi_{LUMO}(k=0)$ and $\psi_{HOMO}(k=0)$ such that they no longer share the structural similarity and consequently exhibit different energies: E_{HOMO} (k=0) $\neq$ E_{LUMO} (k=0). In a similar manner, the HOMO and the LUMO densities of the high disorder DNT structures possess no similarities in their structure (exemplified by DNT1 in Fig. 4.5(a) and (b)) and are also non-degenerate. Structural symmetry of the final atomic structure is thus associated with the presence of the gap.
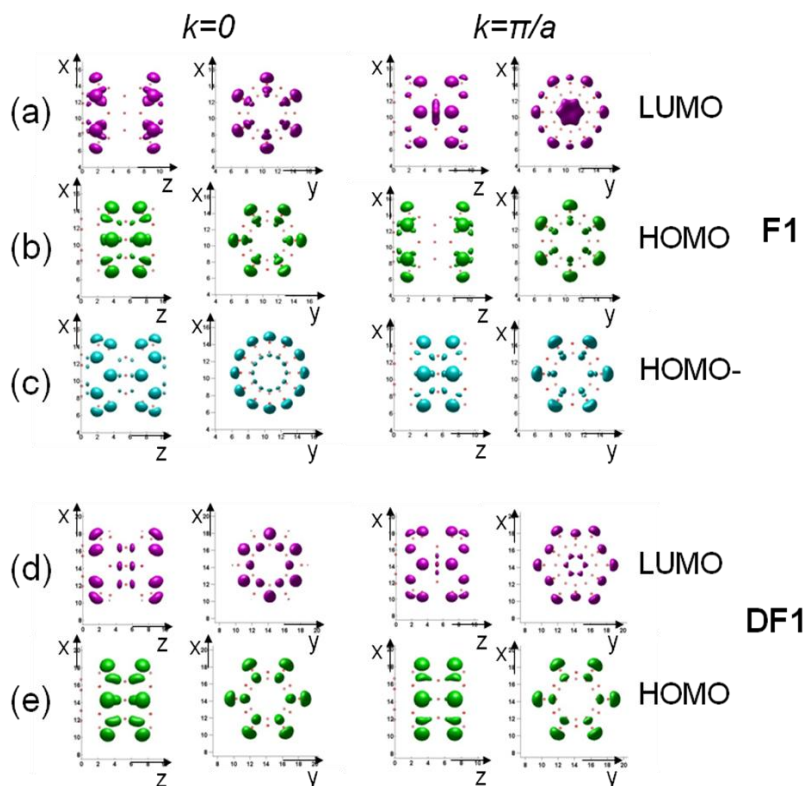
Fig. 4.4 Spatial plot of wavefunction magnitude isosurface (axis of the wire is along z; small red dots represent atomic positions) (a) $|\psi_{LUMO}|=5$ bohr$^{-3/2}$ for F1, (b) $|\psi_{HOMO}|=5$ bohr$^{-3/2}$ for F1, (c) $|\psi_{HOMO-}|=5$ bohr$^{-3/2}$ for F1, (d) $|\psi_{LUMO}|=5$ bohr$^{-3/2}$ for DF1, (e) $|\psi_{HOMO}|=5$ bohr$^{-3/2}$ for DF1
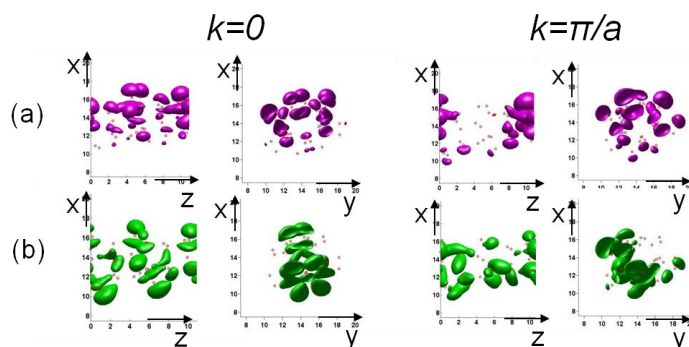
Fig. 4.5 Spatial plot of wavefunction magnitude isosurface (axis of the tube is along z; small red circles represent atomic positions) (a) $|\psi_{LUMO}|=5$ bohr$^{-3/2}$ for DNT1, (b) $|\psi_{HOMO}|=5$ bohr$^{-3/2}$ for DNT1

To understand the aggregate effect of the change in symmetry over all k points, we look at the atomically resolved local density of states (LDOS) for F1 and DF1. First we note that the atoms of F1 lie on two concentric cylinders A and B of symmetrically equivalent atoms, as shown in Fig. 4.6(a). Each of these cylinders splits into two cylinders

in the lower symmetry structure DF1. So, by symmetry, we have only two distinct LDOS plots for F1 but four for DF1. Those for DF1 are shown in Fig. 4.6(b). The reduction in
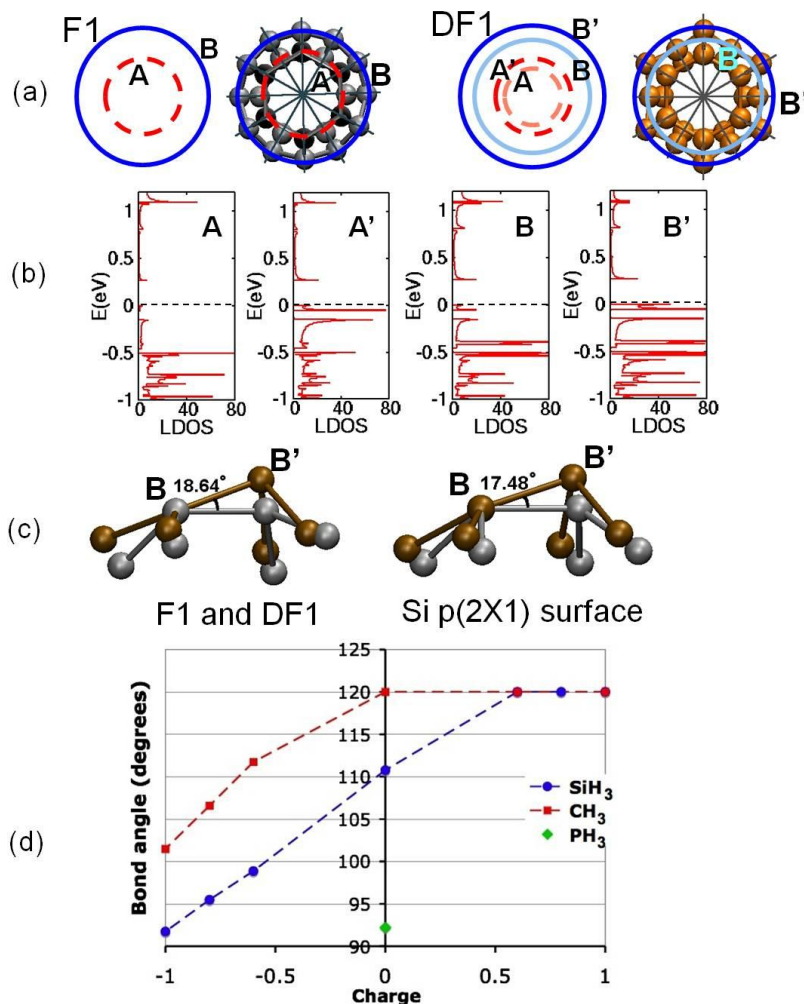
Fig. 4.6 (a) The concentric circles of atomic positions in the cross-sectional view of F1 and DF1, (b) the LDOS within a radial distance of 1.3Å for atoms of DF1 lying on the cross-sectional circles (Fermi level at 0eV) A, A', B and B', (c) comparison of the surface distortion in unpassivated fullerene-like SiNW and Si (100) surface where the gray and brown represent the undistrorted and distorted structures respectively, (d) plot of bond angle versus charge on central atom showing how the bond angles decrease as the central atom acquires negative charge (electrons)

symmetry redistributes the HOMO states among the atoms such that these states now reside almost completely on the atoms of the outer cylinders A' and B' and none on the atoms of the inner cylinders A and B. It is clear here that the change in symmetry separates the atoms into groups of different contributions to the valence band. As a result the outer atoms (on A' and B') acquire a patial charge. If the bond environment of the central Si atom in the trihydride of silicon is studied (fig. 4.6(d)), it is found that as the negative

charge on Si atom is increased, the bond angle between the bonds of Si atom decreases. This is also why the bond angle in the trihydrides decreases as one successively goes from a less electronegative to a more electronegative central atom: C to Si to P. Hence the bond angles surrounding the outer atoms B' are smaller than those on the inner atoms B in DFs and the surface of the wires is distorted. This effect is similar to the Jahn Teller distortion observed on the silicon surface[43, 44] (a comparison of the change in bond environment of the corresponding dimers on DF1 and on reconstructed Si(100) surface is done in figure 4.5(c) and table 4.2) and also explains why the low symmetry structures are more stable.

Table 4.2 Table listing the bond-angles around Si(100) (symmetric and asymmetric) surface, fullerene 1 (F1 and DF1) and fullerene 2 (F2 and DF2'') dimers

	Si(100) p(2X1) surface		Fullerene 1		Fullerene 2	
Atom	Sym	Asym	F1	DF1	F2	DF2''
Inner atom	107.50°	122.41°	112.31°	118.82°	113.30°	120.62°
	112.40°	111.34°	112.31°	118.82°	113.28°	120.53°
	107.50°	122.41°	104.88°	121.37°	105.20°	118.13°
Outer atom	107.50°	88.38°	104.87°	85.41°	105.11°	87.78°
	112.40°	106.82°	112.30°	95.68°	113.23°	95.88°
	107.50°	88.38°	112.32°	95.68°	113.21°	95.89°

4.2.3 Band structures of H-passivated small diameter silicon nanowires

The K-S bandstructures of H passivated tubes from DFT-GGA reported in Fig. 4.6 and the bandgaps specified in Table 4.3 show that in all cases, the band gap increases from unpassivated to the passivated structures in a manner similar to what has been observed for diamond core wires.[39] However, this increase is much higher for DF2' and DF1 than for DNT1. This can be attributed to the fact that DNT1 originally carries less dangling bonds (12) than DF2'(20) or DF1(24) and also to the significant change in bond angles at the surface of DF2' or DF1 when H passivated. Table 4.3 also shows that the bandgaps of the H passivated fullerene tubes are higher than those of the bulk-like wires of similar diameter while that of the DNTs are lower. This could mean that the true bandgaps of the H-passivated DNTs lie within the visible spectrum range while those of the H-passivated DFs lie well outside that range. The bandgaps of the diamond like wires of similar

diameters lie towards the violet end of the spectrum. It is also interesting to note that on hydrogen passivation, both DFs and DNTs transform to indirect bandgap materials.
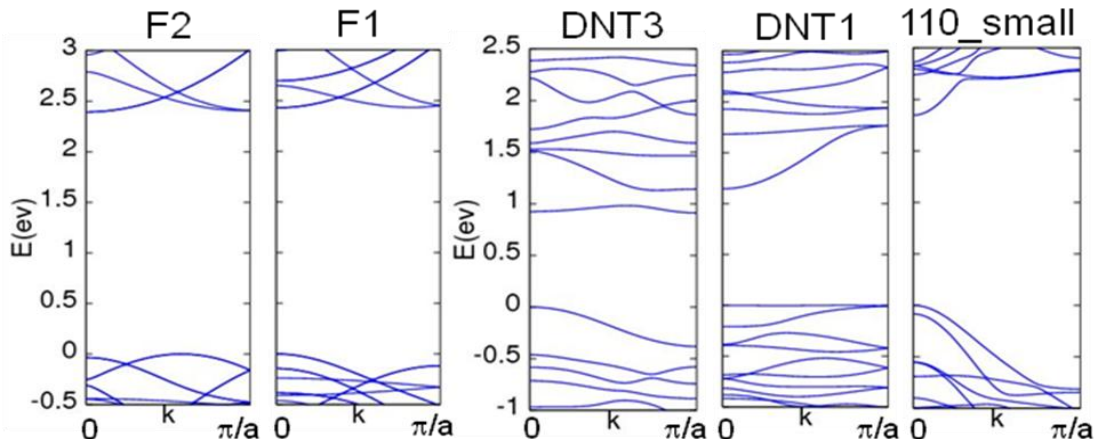
Fig. 4.7 K-S bandstructures of the passivated silicon nanowires of very small diameter

Table 4.3 Table listing the unit lengths ɑ, formation energies ε (calculated by equation (3.2)), the Kohn-Sham energy band gap E_g from DFT-GGA, direct(D)/ indirect(I) nature of gap and the electron and hole effective masses of the ~1nm diameter hydrogen passivated 1-D silicon nanostructures shown in figure 3.4 (NC = not calculated)

Structure	ɑ (Å)	ε (eV)	K-S E_g from DFT-GGA (eV)	D/I	m_e^*/m_0	m_h^*/m_0
DNT1	11.10	0.788	1.145	I	0.23	5.34
DNT3	9.90	0.870	0.912	I	1.18	0.45
F2	10.50	0.827	2.393	I	0.53	0.40
F1	10.20	0.829	2.429	D	0.56	0.40
110_small	7.60	0.734	1.846	D	0.13	0.21
110_big	7.60	0.593	NC	NC	NC	NC
111	18.93	0.792	2.253	NC	NC	NC
112	13.40	0.948	1.825	NC	NC	NC

Table 4.3 also shows that the effective masses of the wires change dramatically on hydrogen passivation. The carrier selectivity is reduced for the fullerene wires. The favored carrier for all wires may now be different from the unpassivated case, but has a lower effective mass, even though this mass is still high compared to [110] bulk-like wire.

4.3 Mechanical response of small diameter unpassivated silicon nanowires

4.3.1 Strength

ReaxFF dynamics of small diameter silicon nanowires as the wires are strained at a rate of 0.04167%/ps show that these wires have very high strengths compared to silicon bulk. For example, fig. 4.8 shows the MD of the fullerene wire F1. The figure shows that the wire can sustain upto 6% strain. This is very high compared to only 0.04% for silicon bulk.
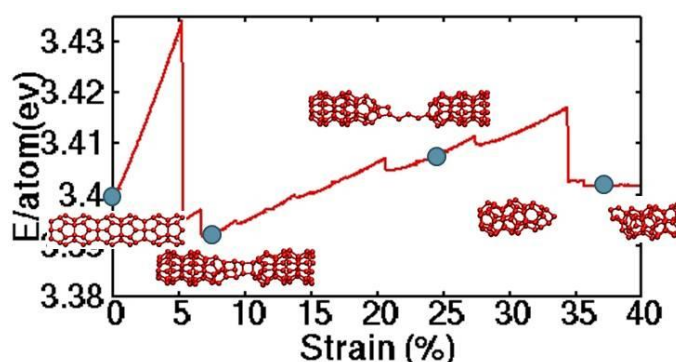
Fig. 4.8 Straining of F1 wire in ReaxFF shows its high strength compared to Si bulk

4.3.2 Young's moduli

Young's moduli for the wires can be obtained from length optimization in DFT, as shown in figure 3.4. The Young's modulus is given by the second derivative of energy per unit area with respect to the length of the tube. As described earlier in section 3.3, a conservative (larger diameter) estimation of the area of the tube has been used. Table 4.3 lists the Young's moduli of the various tubes as obtained from SeqQuest simulations. The results show that even though the tubes are energetically comparable, their Young's moduli can differ by as much as a factor of 2. We, therefore, have several nanotube structures with similar energetics but varying elastic and electronic properties.

Table 4.4 The unit lengths L, cross-sectional areas A, energies per atom from SeqQuest ε_S and the Young's moduli E from DFT-GGA of the unpassivated nanowires

Structure	L (Å)	A (Å^2)	ε_S (eV)	E (GPa)
DF1	10.64	80.9	0.638	118
DNT1	11.12	81.8	0.658	72

DNT2	10.58	86.0	0.673	86
F1	10.86	72.2	0.705	145
DNT3	9.79	69.4	0.708	50
F2	10.97	57.9	0.714	179
Pen	2.42	33.3	0.755	273
Hex	2.40	40.7	0.774	493
CNT (4,4)	3.89	324.7	0.805	53
SHW1	2.49	90.2	0.663	305
SHW2	2.64	40.7	0.751	140

4.4 Conclusions

In summary, while the previous chapter used longer time scale simulations with reactive force field to explore stable SiNT structures of diameter less than 1 nm, the current chapter used density functional theory to calculate electronic band structures and Young's moduli of these structures.

1.   The clean distorted fullerene and distorted nanotubes are perhaps the only SiNW structures reported at these dimensions which consistently show a small band gap.

2.   The bandgaps in the clean tubes can be associated with the symmetry loss and disorder in their structures and their stability, akin to asymmetrically reconstructed Si(100) surface.

3.   On hydrogen passivation, the bandgaps of all nanotubes increase, but the increase is much larger for the DFs than the DNTs. The K-S bandgaps are smaller than those of the diamond-core wires, and the true bandgaps are likely to fall in the optical spectrum.

4.   The effective masses of the DNTs are high compared to diamond-core wires.

5.   The DFs possess higher Young's moduli compared to the DNTs.

5. SIMULATING REALISTIC NANOSTRUCTURES WITH DIMENSIONS OF SEVERAL NANOMETERS

It was mentioned in chapter 1 that a driving force behind the use and development of atomistic simulations is to be able to simulate larger systems using a bottom up approach. To demonstrate how the methods described hitherto can be applied for the simulation of a realistic larger device, the thesis uses the case of strained-Si/ strained-Ge/ strained-Si nanowires of the form shown in figure 5.1(a). These structures with widths ranging from 30-300 nm have been fabricated by the Hoyt group at M.I.T.,[15]. A theoretical study of the structural aspects of such structures has been carried out using ReaxFF by Park *et al.*[16] They varied the height H and the width W of the Ge layer in the nanostructure. The other dimensional measurements depicted in Fig. 5.1(a) are the same as simulated by Park *et al.* The height of the Ge layer was large compared to the heights
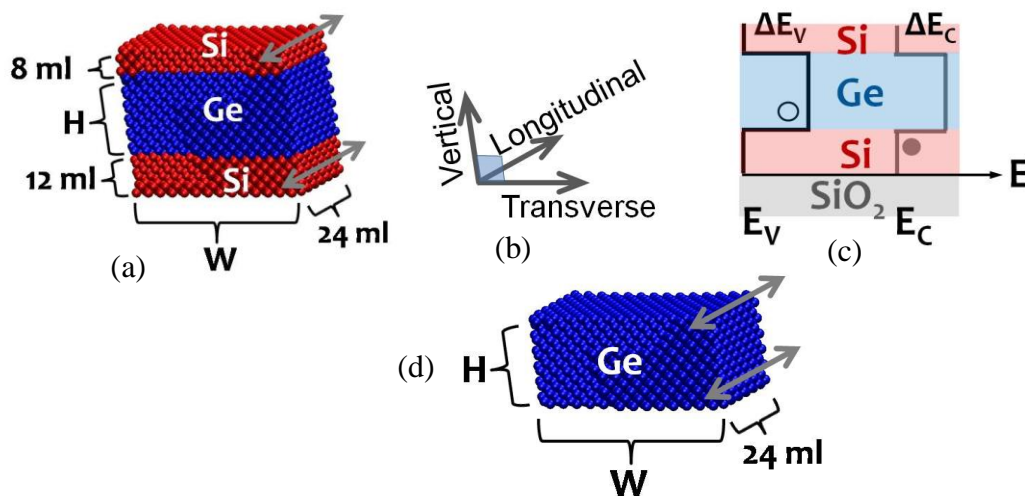
Fig. 5.1 (a) The studied strained-Si/ strained-Ge/ strained-Si nanobars, (b) the defined directions, (c) the band-edge lineup in the bars, (d) the actual simulated germanium section of the bars

of the Si sections. Owing to the substantially large Ge section compared to the Si sections in the hetero-structures and also the confinement of holes in the Ge section as shown in fig. 5.1(c), this thesis focuses on the germanium sections (fig. 5.1(d)) of the hetero-

structures and primarily studies their hole properties. So, in effect, realistically strained germanium <100> wires are studied here.

5.1 Background

5.1.1 Strain engineering in semiconductor devices

In recent years, strain has been increasingly employed by the semiconductor industry to enhance carrier mobilities (μ_{eff}) in the channel of the MOSFET. It is also being investigated for improvements in the current gain (β) and the maximum oscillation frequency (f_{max}) of the BJT[45] or HBT[46]. In industry, strain has been incorporated in MOSFETs using process-induced stressors. But strain in a material can also be introduced by growing it epitaxially on another relaxed material (referred to as virtual substrate) with the same crystalline symmetry but a different lattice parameter. For example, silicon grown epitaxially on top of relaxed $Si_{1-x}Ge_x$, which has larger bond length, will be strained to a degree that can be controlled by the composition of Ge, x in the alloy. A defect free interface is ensured by controlling the height of the grown layer to remain less than a certain thickness called the critical thickness. The critical thickness depends on the amount of strain introduced in the grown silicon and hence on the Ge composition of the virtual substrate.

To consider how strain effects improve mobility, let us consider the example of strained silicon. The hydrostatic component of the strain introduces a positive (compressive) or negative (tensile) energy band shift, while the uniaxial component results in a splitting of the conduction and valence band degeneracies with the strain direction CB valley Δ_2 and the heavy hole VB slipping (uniaxial compression) or rising (tension) in energy.[47] In the tensile biaxially strained Si, electrons preferentially occupy the lower energy Δ_2 conduction band, which has smaller in-plane effective mass calculated by averaging over all six valleys. In addition, intervalley scattering is suppressed by the conduction band energy splitting. Both these effects contribute to enhanced electron mobility.

Asymmetric in-plane strain configurations can lead to the largest transport enhancements.[48, 49] To achieve uniaxial strain configurations in Ge, which is of particular interest due to high hole mobility, Hashemi *et al.* have fabricated strained-Si/ strained-Ge/ strained-Si (s-Si/s-Ge/s-Si) hetero nano-bars on insulator. They study the interplay of the thickness, width and lateral strain relaxation of the Ge film. [15]

5.2 Case study – strained Si/ strained Ge/ strained Si on insulator hetero nanobars

5.2.1 Study of strain in fabricated s-Si/ s-Ge/ s-Si heterostructure (Hashemi *et al.*)

Hashemi *et al.* [15] grow relaxed s-Si/s-Ge/s-Si heterostructure on a relaxed SiGe virtual substrate such that the starting material has symmetrically biaxial strain in both Si (~2% tension) and Ge (~2% compression). The thin-body heterostructure is bonded to the SiO_2 substrate, the back SiGe is removed and the exposed s-Si cap layer is thinned. The heterostructure-on-insulator (HOI) substrates are then patterned into stripes with widths ranging from 30-300 nm. As the stripes become narrower and the s-Si cap layer thicker, the authors observe enhanced tensile strain in the cap layer. The transverse compressive stress in Ge is reduced by narrowing the bar width.

5.2.2 Structural simulations with ReaxFF MD (Park *et al.*)

To obtain the realistic hetero-structure wires computationally, Park *et al.* carried out molecular dynamics of the heterowires shown in fig 5.1(a) [16] using the reactive force field ReaxFF also used earlier in this thesis, in chapter 3, to explore SiNT structures. The bottom Si layer was fixed at ~2% biaxial tension and the Ge layer was ~2% biaxially compressed. Dynamics of the heterowires at 10K led to relaxed structures while dynamics at 300K provided reconstructed structures. The authors observed that the average compressive transverse strain in the Ge layer is relaxed as the bar width is reduced or the Ge height is increased. Structures with square Ge cross-sections exhibited approximately uniaxial strain in the Ge layer. An important observation of Park *et al.* is the enhancement of transverse strain relaxation due to surface reconstruction for Ge layers with larger heights. Their results show 44.5 % relaxation for the geometry for which Hashemi *et al.* estimated 45% transverse stain from Raman spectroscopy, thus establishing validity of the structures obtained from ReaxFF.

5.2.3 Energy band lineup in s-Si/ s-Ge/ s-Si hetero- nanobars

The heterostructure is often conceived within macroscopic models, such as the electron affinity rule, as being built by joining bulk strained silicon and germanium layers. Then the band lineup such as the one shown in Fig. 5.1(c) can be obtained by calculating the band edges and thereby ΔE_C and ΔE_V for strained germanium and silicon bulk using sp^3d^5s* tight binding and the strain model by Boykin *et al.*[21] The conduction band valley for Ge occurs at L point, while the conduction band valley for Si occurs along the <100>

($\Gamma\rightarrow\Delta$) k-path. The VB edge is defined by the light hole band maximum. Considering the cases of biaxial and uniaxial strains:

1. Biaxial case: the strains considered are $\varepsilon_x = 0.021$, $\varepsilon_y = 0.021$, $\varepsilon_z = 0.01633$ for Si and $\varepsilon_x = -0.0201$, $\varepsilon_y = -0.0201$, $\varepsilon_z = 0.014124$ for Ge. $\Delta E_C = 0.4285$ eV, $\Delta E_V = 0.64036$ eV.

2. Uniaxial case: the strains considered are $\varepsilon_x = 0.005434$, $\varepsilon_y = -0.0201$, $\varepsilon_z = 0.005434$ for Ge and $\varepsilon_x = 0.04745$, $\varepsilon_y = 0.020016$, $\varepsilon_z = -0.026237$ for Si. $\Delta E_C = 0.45274$ eV , $\Delta E_V = 0.5384$ eV.

However, for unstrained bulk, the method used here (tight binding) over-estimates both ΔE_C and ΔE_C by 0.26 eV compared to those obtained by the Anderson (electron affinity) rule, which are also the experimentally observed values. Hence, it is possible that the values obtained here are also over-estimated.

5.3 Tight binding simulations of strained hetero-nanobars

The study reported here starts with the realistically relaxed 1-D s-Si/s-Ge/s-Si {100} hetero-structures (fig. 5.1(a)) with Si-cap (top) layer of 8 monolayers (~2.1nm) obtained from ReaxFF.[16] Two heights (H) of the germanium layer are studied: 48 monolayers (~7nm) and 72 monolayers (~10nm). The widths (W) of the hetero-structures range from 56 monolayers (~8nm) to 296 monolayers (~41.5nm). The unit length (L_0) of all the wires is 24 monolayers (~3.3nm) in the longitudinal (periodic) direction. As discussed earlier, in the periodic longitudinal direction the nanobar is constrained to have 2% average compression in germanium and 2% average expansion in silicon. These strain constraints are introduced to mimic the experimentally fabricated structures. In the other two directions, there are no constraints during MD and the atoms are allowed to relax their positions. To avoid the effects of surface reconstruction, this thesis studies relaxed rather than reconstructed hetero-structures.

Owing to the substantially large size of the Ge section compared to (>2.4 times) the Si sections in the hetero-structures and to the confinement of holes in the Ge section, this study focuses on the germanium section of the hetero-structures and their hole properties (to be discussed further in section 5.3.1). In effect, therefore, this thesis studies realistically strained germanium <100> wires. These wires shall henceforth be identified by (H,W) where H and W are the height and width dimensions respectively in nm. The strains in these realistic wires are not uniform and vary from bond to bond within the wire. The

transverse strain variation is shown in figure 5.2(a) for wire of height ~7nm and width 8.2nm. The average longitudinal strain in these wires is fixed at ~2.08% compression, but the average compressive transverse strain increases as the wire becomes wider as discussed in ref. [16]. It should be noted here that if the wires were homogeneous (uniform strain), the plot of the kind shown in fig. 5.2(a) would collapse to a single point at the average transverse strain. Fig. 5.2(b) summarizes the transverse strain data for the five studied MD relaxed wires of height ~7nm. This study compares the realistic MD relaxed non-homogeneously strained wires with homogeneous <100> germanium wires of same dimensions (in terms of monolayers of atoms). The comparison is performed against unstrained, uniaxially compressively strained and biaxially compressively strained wires. Even when the four kinds of wires carry the same number of monolayers in every direction, they have slightly disparate dimensions owing to the different strains. The H and W used to indetify the wires would therefore be the approximate rounded dimensions. Because the wires are made up of an integer number of 8-atom cubic unit cells of germanium in each directon, it is straightforward to know the exact dimensions from these approximate dimensions if the strains are known.
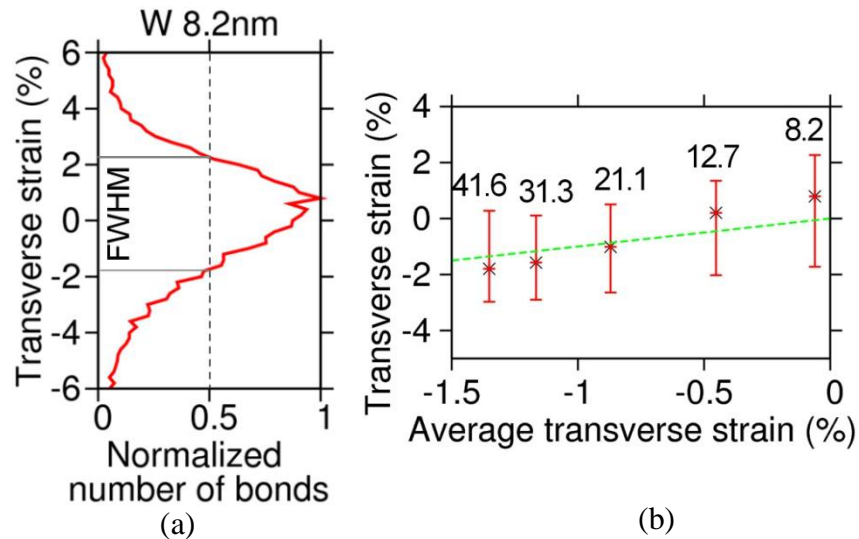
Fig. 5.2 (a) Variation of the number of bonds with a particular transverse strain in the 7nm high, 8.2nm wide wire showing the full-width at half-maximum (FWHM) strain range. (b) Data of all the MD relaxed wires identified by the widths shown on the plot, against the average transverse strain showing the full-width at half-maximum (FWHM) strain range for the number of bonds and the strain exhibited by the peak number of bonds. The dotted line represents the average strain.

The electronic structures are calculated using $sp^3d^5s^*$ tight-binding with bulk Ge parameters obtained from genetic algorithm fits.[20] Strain corrections suggested by

Boykin *et al.* [21] are applied for all strained bonds. The surface atom dangling bonds are "passivated" by modifying the atom parameters as suggested by Lee *et al.*[50] The eigenvalues of the tight binding Hamiltonian were evaluated using Lanczos solver. To obtain the degeneracies, Block Lanczos algorithm with block size of 6 was used. The code used for this study is a modified version of the basic NEMO-3D.[51] The code was modified to enable calculations for arbitrary atomic geometry, such that the structures obtained from ReaxFF could be simulated.

Since the wire unit cells are six times longer (6 times replicated) in the longitudinal direction than the 8-atom bulk Si cubic unit cell, the Brillouin zone of the wires is $\pi/(6a)$ where a represents the bulk Si cubic unit cell constant. Energy eigenvalues are calculated at 26 equispaced k points from 0 to $\pi/(6a)$. It must be noted that because these wire bands are 6 times folded versions of those of a non-replicated wire with unit length equal to that of 8-atom cubic unit cell, the conduction band minima that appear to exist at k=0 in the 6 time replicated wires actually occur at k=π/a for a non-replicated wire.

To calculate the electron or hole conductivity (or curvature) effective masses of the wires, we average over the electronic states assuming occupancy of the conduction or valence bands, respectively, according to Boltzmann statistics for non-degenerate semiconductor:

$$m_c* = \left(\frac{\sum_i \sum_j \frac{1}{\hbar^2} \frac{d^2E}{dk^2}\bigg|_{ij} e^{-E_{ij}/k_BT}}{\sum_i \sum_j e^{-E_{ij}/k_BT}} \right)^{-1} \tag{5.1}$$

where m_c* is the curvature (conductivity) effective mass, ij represents the jth k point in the ith conduction or valence band, E is the energy eigenvalue, k is the wavenumber, T is the temperature (300K) and $\hbar$ and k_B are the universal Planck and Boltzmann constants respectively. It should be noted that the degeneracies are taken into account when summing over the bands i, and that the discrete summation over E values calculated at regular k intervals takes care of the density of states (DOS) in equation (5.1). The m_c* thus defined is the effective mass that yields the low-bias steady-state mobility assuming an energy-independent scattering relaxation time.

The DOS hole effective masses can also be calculated. It has been suggested earlier [52] that instead of including the Boltzmann statistics over all energies for non-degenerate semiconductor as done in (5.1), one could alternatively calculate the DOS effective mass for ith band only at $E=E_{ij}$ such that $(E_{V0i}- E_{ij})=E_{th}$ (the thermal energy),

where E_{V0i} is the maximum energy of the ith subband, and obtain the DOS effective mass with a very small error ($<1\%$). Using this approximation, the DOS effective mass for the ith subband is given by:

$$m_{di}* = \frac{\hbar^2 E_{th}}{2}\left[\sum_j \left|\frac{dE_i}{dk}\right|^{-1}_{k=k_j} \delta(E_{ij} - E_{V0i} + E_{th})\right]^2 \tag{5.2}$$

where $m_{di}*$ is the DOS effective mass for subband i and k_j, indexed by j, represents the k points.

### 5.3.1 Rationale of studying only germanium sections of the wires
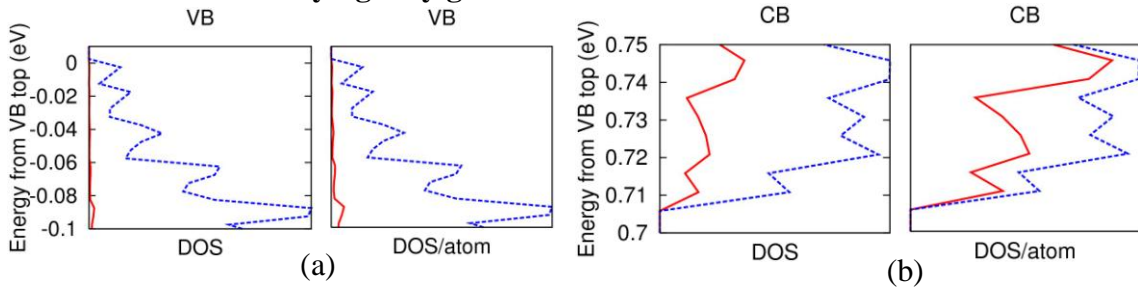
Fig. 5.3 Total density of states (DOS) and DOS per atom contributions from germanium (blue dotted) and silicon (red solid) atoms in (a)valence band and (b)conduction band of a homogeneous (7,21) wire with average strains equal to that of corresponding MD relaxed wire; all energies are referenced to VB maximum in the wire

It has been mentioned earlier that the rationale for studying only germanium sections here is based on two arguments: the higher valence band edge and lower conduction band edge in germanium as compared to silicon and the the larger number (>2.4 times) of germanium atoms compared to silicon atoms. However, as was discussed earlier in section 5.2.3, the band lineup obtained from applying tight binding to bulk material is not necessarily accurate. So this argument should be verified true. A simple way to take into account both the above mentioned factors in a single check is to investigate the atomically-resolved density of states (DOS) in the wires and compare the contribution of all silicon and all germanium atoms. As an example, figure 5.3 does this for a homogeneous (7,21) wire with average strains in all directions the same as in the corresponding MD relaxed wire. The plots in the figure show that the total and per atom contribution from silicon atoms to valence band states within the first 0.1eV from the valence band edge of the wire is negligible compared to the contribution from the germanium atoms. This is however not true for the conduction band (for unstrained bulk,

ΔE_C is known to be only about 0.05eV and strain causes splitting of the conduction bands). These results lead us to the conclusions that because the holes are confined in the thick germanium layer, this structure can be used to construct a p-type device and that the valence band and hole properties can be safely studied by considering only the germanium section.

5.3.2 Confinement effect in unstrained germanium

By assuming the longitudinal periodic direction of a hypothetical unstrained germanium [001] wire (see fig. 5.1(b)) to be the $\hat{k}_z$ direction, the effect of confinement on the band properties (band edges and band curvatures) along this k direction ($\hat{k}_z$) can be studied. Germanium bulk has CB minimum at L symmetry point $(k_x, k_y, k_z) = (\pi/a, \pi/a, \pi/a)$ in the Brillouin zone, where a is the lattice constant of the 8-atom cubic unit cell. The next conduction band valley for Ge bulk occurs at Γ point. The VB maximum is at Γ point (0,0,0) where the light hole band and the heavy hole band are degenerate. The k-path of interest for electron effective mass here would be $(\pi/a, \pi/a, 0)$ to $(\pi/a, \pi/a, \pi/a)$ and for hole effective mass would be $(0, 0, 0)$ to $(0, 0, \pi/a)$. As one limits the x-dimension (say) to give a (100) slab of thickness L_x, the E values get sampled at intervals of $2\pi/L_x$ along the $\hat{k}_x$ direction of the bulk and all these sampled values get projected on to the $\hat{k}_y$ -$\hat{k}_z$ plane as subbands. For the slab, the k-path of interest for investigating the electron effective mass would then be $(\pi/a, \pi/a, 0)$ to $(\pi/a, \pi/a, \pi/a)$ and for investigating the hole effective mass m would be $(0, 0, 0)$ to $(0, 0, \pi/a)$. Finally, for the wire the y-dimension is also limited. As a result, for the wire, the E values in the slab get sampled at intervals of $2\pi/L_y$ along the $\hat{k}_y$ direction and all these sampled values get projected on to the $\hat{k}_z$ direction, which is the only k-path left to study the dispersion along in the wire.

In figure 5.4, the cases of a germanium slab with L_x = 7nm and a germanium wire with L_x = 7nm, L_y = 8nm are considered and compared with germanium bulk. The shifts in the conduction and valence band edges, the corresponding increase in the bandgap and the degradation in the curvature effective masses are clearly evident in figures 5.4(a) and (b) as one goes from bulk to slab and then slab to wire. The results for the band edges are summed up in figure 5.4(c) and for the effective masses in figure 5.4(d). If the discussion here is extended to wires, one would expect the bandgaps to increase and the effective masses to increase as one reduces the coss-section of the wires. Such results have been reported in [53] and [54].
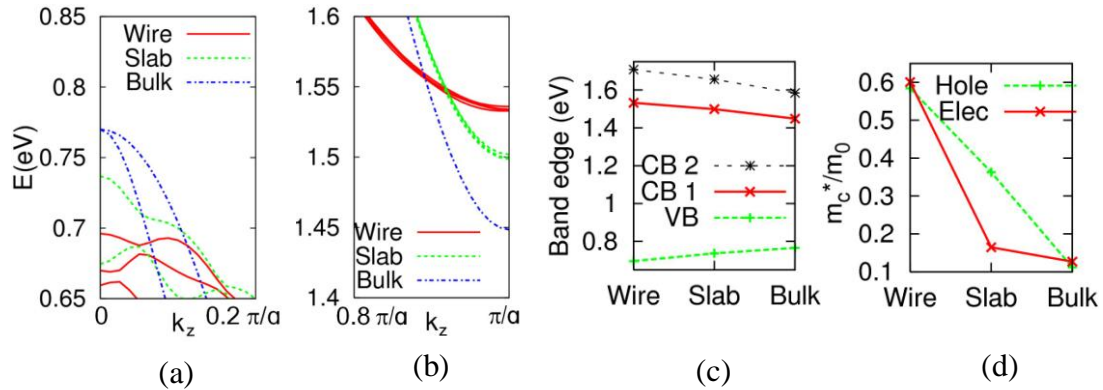
Fig. 5.4 (a) Valence bands at the lowest valley, (b) conduction bands at Γ along $\hat{k}_z$ of germanium bulk, a germanium slab limited to 7nm in the x-direction and a germanium wire limited to 7nm in the x-direction and 8nm in the y-direction. (c) The valence band and the two lowest conduction band edges for germanium bulk, slab and wire. (d) The hole and electron (elec) curvature effective masses for germanium bulk, slab and wire.

5.3.3 Tight binding calculations of germanium wires
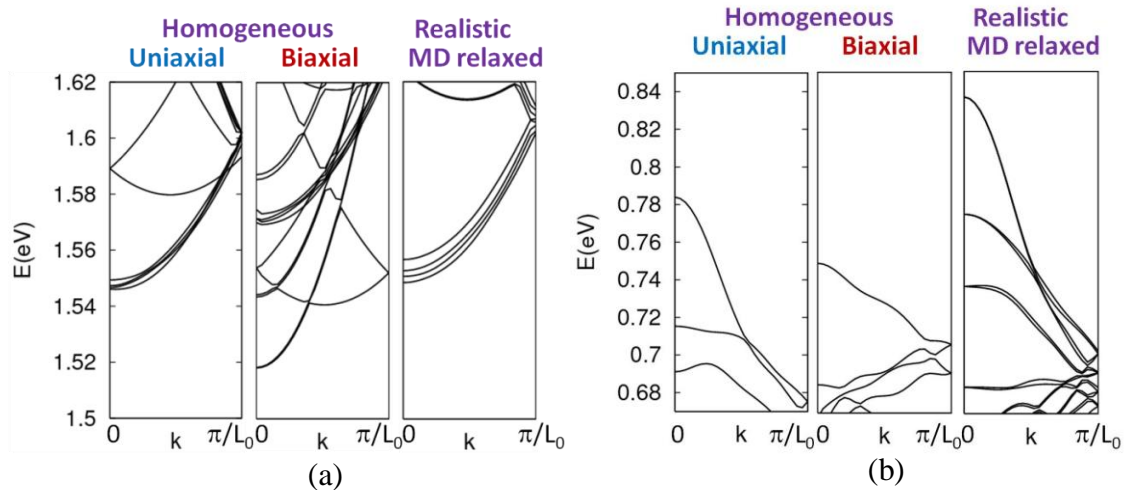
Fig. 5.5 (a) Conduction bands and (b) valence bands for homogneoeusly strained and MD relaxed (7,8) wire.

Figure 5.5 compares the effect of different strain conditions (hypothetical uniformly uniaxial strain, uniformly biaxial strain and realistic strain obtained from MD relaxation) on (7,8) wire. The conduction and valence bands of the homogeneous uniaxially, homogeneous biaxially and the non-homogeneous MD relaxed wires differ in both band edge locations and the band curvatures (effective masses). The valence band radius of curvatures appear to be substantially enhanced for the homogeneously uniaxially

strained and the MD relaxed wire compared to the unstrained and the homogeneously biaxially strained wires.

5.3.4 Band edges and bandgaps

As discussed in 5.3.2, an increase in the bandgap is expected as the wire cross-section is reduced. Evidence for this in experimental and theoretical literature for silicon nanowires was discussed earlier in 3.1.1.
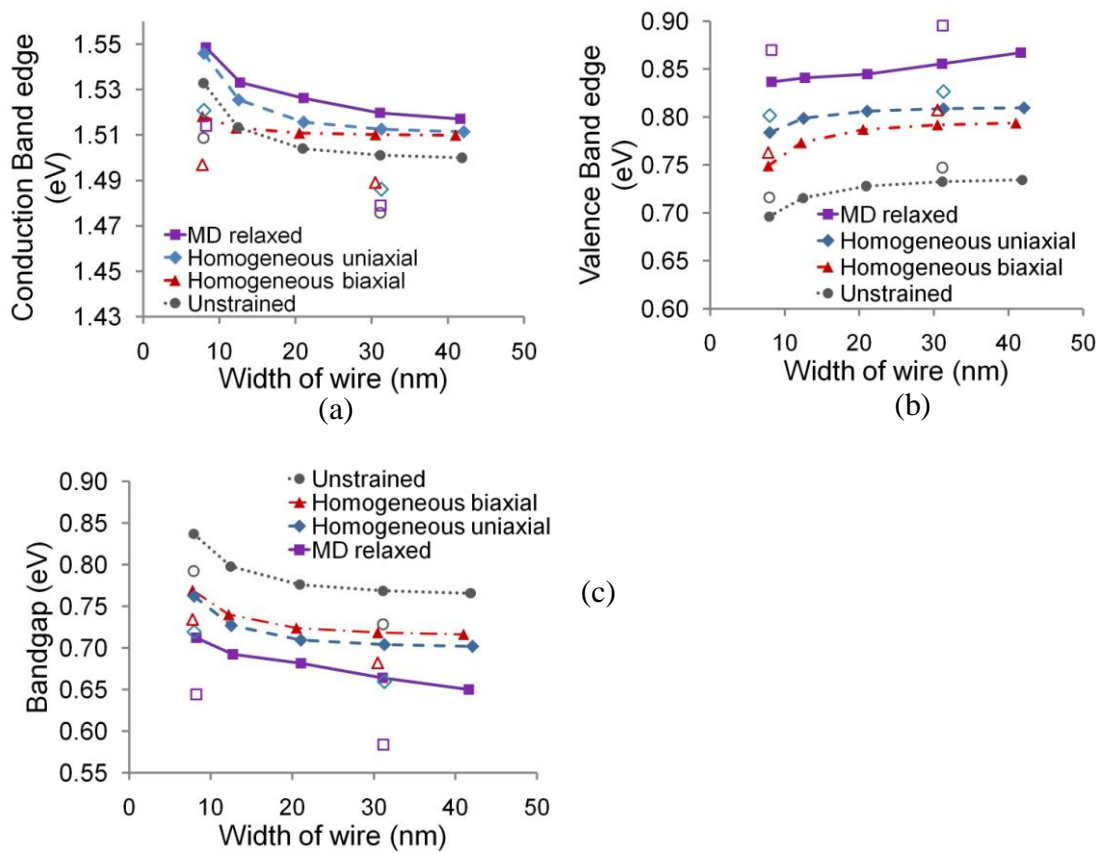
Fig. 5.6 (a) Conduction band edges, (b) Valence band edges and (c) Bandgaps in the simulated germanium wires of height ~7nm (filled markers) and ~10nm (open markers)

Figures 5.6(a) and (b) show respectively the shifts in the conduction and valence band edges as W is increased for (7,W) [solid markers] and (10,W) [open markers] wires. As expected, it is observed that owing to confinement, for a given wire height, band gap (fig. 5.6(c)) increases as the wire width decreases for the realistic MD relaxed wires as well as the homogeneously strained biaxial or uniaxial wires. It should be noted that strain causes all bandgaps to decrease, the decrease is higher for the homogeneous uniaxially

strained than for the homogeneous biaxially strained wire. However, the bandgap for the non-homogeneously strained MD relaxed wires is the smallest (smaller by about 0.1eV from hypothetical unstrained wire) for all sizes. A key point to note here is that conduction band of the germanium wires is weakly dependent on the strain conditions compared to the valence band.

5.3.5 Curvature electron effective masses

The curvature of the lowest conduction band is shown in figure 5.7 (a) for all the wires. It should be noted that owing to switch in the order of the bands near the edge as the size of the wire is changed, we fail to see the pattern of increasing effective mass with decreasing wire cross-section expected from the simple bulk→slab→wire discussion. The average curvature effective mass (fig. 5.7 (b)) for the MD relaxed wire is higher than the uniform wires and shows a behavior mixed of the behaviors exhibited by the uniform uniaxially and biaxially strained wires. The average electron effective mass of the MD relaxed wire remains close to the uniaxially strained wire masses for the sizes simulated.
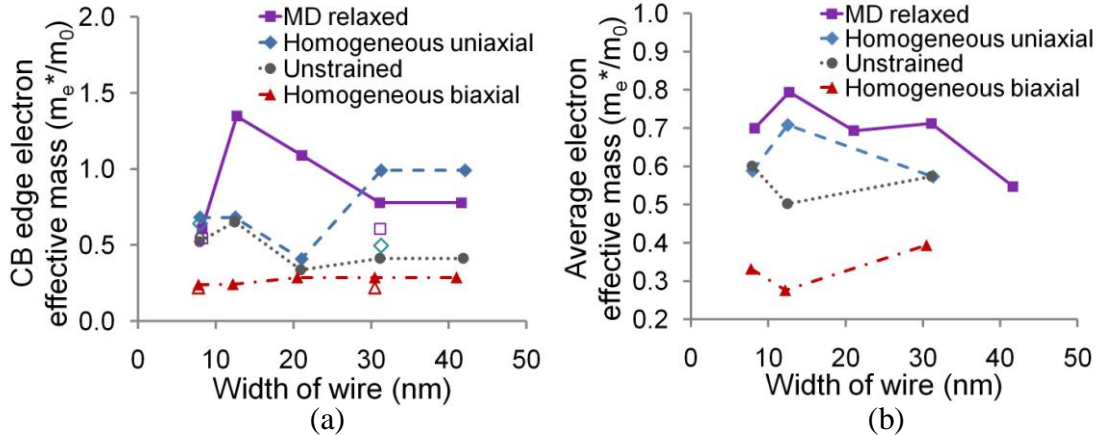
Fig. 5.7 (a) The curvature electron effective masses of the lowest conduction band at the conduction band edge and (b) the average curvature electron effective masses of the ~7nm (filled markers) and ~10nm (open markers) germanium wires

5.3.6 Curvature hole effective masses

Figs. 5.8(a) and 5.8(b) show the valence band edge curvature hole effective mass and the average hole effective mass calculated by using equation (5.1). The hole effective mass is well-behaved with a regular trend with the cross-sectional size of the wire. For the uniform uniaxially or biaxially strained wires, this trend is what would be expected from

the discussion in section 5.3.2. However, for the MD relaxed wires, the trend obtained is opposite, i.e., the hole effective mass decreases with decreasing wire cross-sectional area.
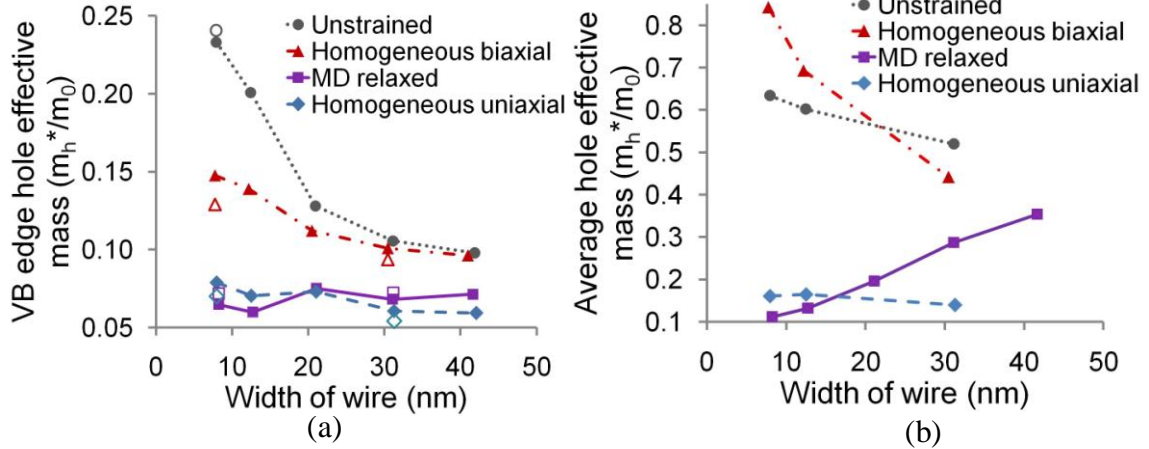

Fig. 5.8 (a) The curvature hole effective masses of the highest valence band at the conduction band edge and (b) the average curvature electron effective masses of the ~7nm (filled markers) and ~10nm (open markers) germanium wires

Fig 5.8(b) shows that for small widths, the MD relaxed wire behaves as a uniformly uniaxially strained wire with regard to its average hole effective mass. The average hole effective mass increases (deteriorates) as the width is increased. The bandstructures in figure 5.9(a) for the MD relaxed wire (7,W) show that though there is little change in the curvature of the valence band edge (which are close to those of the uniformly uniaxial wires as seen in figure 5.8 (a)) as W is increased, the valence subbands cave in faster to become concave upwards than do the subbands in the uniaxial wires (shown for (7,31) wire in figure 5.9(c)). This leads: (a) the slope |dE/dk| to reduce as the bands bend upwards resulting in an increased density of states and hence a measurable influence on the average effective mass even when the states are far from the band edge, (b) the curvature of the band to change its direction, thereby contributing a negative hole effective mass. These two factors together deteriorate the average hole effective mass in the MD relaxed wires for higher widths. Thus, as shown in figure 5.9(a), for the (7,13) wire, the valence bands of MD relaxed wire are similar to the valence bands of the uniformly uniaxially strained wire, while for the (7,31) wire, the valence bands of the MD relaxed wire possess likeness to the valence bands of the uniformly biaxially strained wire (fig. 5.9(c)).

It should be noted here that the similarity of the MD relaxed small width wires to uniaxially strained wires while that of the larger width MD relaxed wires to biaxially strained wires of equivalent dimensions in terms of their bandstructure and effective mass

is reminiscent of the fact that the smaller width wires have an average strain that is almost uniaxial while the larger width wires have an average strain that is biaxial as discussed in section 5.2.2. Two natural questions arise at this point: Are the electronic bandstructure properties of the MD relaxed wires driven by the nature of their average strain? Is the non-uniformity of strain in the MD relaxed wires important?
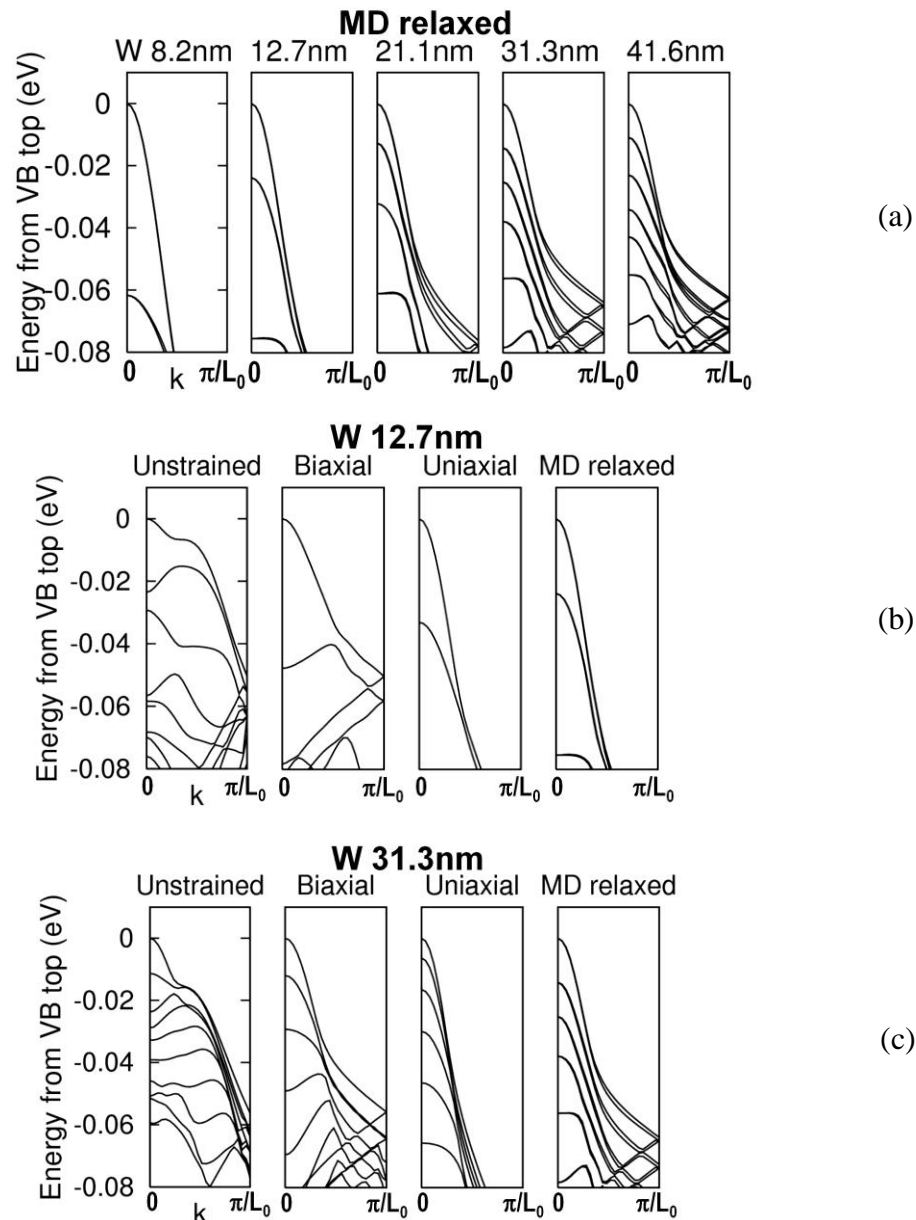

Fig. 5.9 Calculated valence bands, referenced to the band top edge as 0eV, of (a) the simulated MD relaxed wires with height ~7nm (the widths are represented above the plots), (b) the ~13nm wide wire of all strains and (c) the ~31nm wide wire of all strains.

5.3.7 Sub-bands and electronic states

The various subbands owing to the confinement (sampling of the E values in the confined directions in k space) are clearly visible in the bandstructures shown in figure 5.8. The states at a given energy may come from one or more subbands. The broader net spatial nature (without atomic-level details) of the wavefunctions in the various sub-bands at a given energy is reflected by the atomically-resolved density of states.

The atomically-resolved density of states from the TB single-particle eigenfunctions is obtained as:

$$ADOS_a(E) = \frac{\sum_i \sum_{b_a} \psi_{ib_a}^2 \left[H\left(E_i - E + \frac{\delta E}{2} \right) - H\left(E_i - E - \frac{\delta E}{2} \right) \right]}{\delta E} \qquad (5.3)$$

where $ADOS_a(E)$ represents the atomically-resolved density of states at discrete energy E and atom a, i indexes the various eigenstates, δE is the energy bin size, b_a represents the atomic orbital basis functions centered on atom a, ψ_i represents the ith eigenstate and ψ_{iba} represents the component of ψ_i along b_a and H is the Heaviside unit step function. It should be noted that in equation (5.3), the eigenstates (represented by the single index i) have not been identified by the band and k-point as was done earlier in equation (5.1). Also, the degeneracies are taken into account when summing over i. The DOS at each bond can be obtained as:

$$DOS_{ij}(E) = \frac{ADOS_i(E)}{n_i} + \frac{ADOS_j(E)}{n_j} \qquad (5.4)$$

where $DOS_{ij}(E)$ represents the density of states at the bond ij between atoms i and j, and n_i and n_j represent the coordination number (number of bonds) of atoms i and j respectively.

This section studies spatial distribution of the electronic states along the height and width of the wire. So the $DOS_{ij}(E)$ are averaged over all bonds along the longitudinal direction which lie at the same height and width position in the wire. Fig. 5.10 shows the resulting state distributions in different valence band energy ranges (referenced to VB edge) for the (7,13) wire. For the MD relaxed wire, the strain averaged along the longitudinal direction is also shown.

New subbands show up as one ventures away from the VB edge into the valence band. Each consecutive subband adds states that have multi-modal spatial distribution along the width (transverse modes), with one higher mode than the previous subband. Thus, for the (7,13) wires shown in fig. 5.10, owing to the location of subbands, the MD relaxed wire has DOS whose spatial distributions are similar in form to those of the

uniaxial wire. On the other hand, for the (7,31) wire, the MD relaxed wire has spatial distributions that are similar to the biaxial wire. However, in either case, the distributions of the MD relaxed wires are not the same as the homogeneous uniaxial or biaxial cases, rather there is a significant difference in the magnitudes. In other words, the distribution of the states in the wires is dependent on the nature of strain in the wire but appears to be dependent on factors other than just the nature of strain.
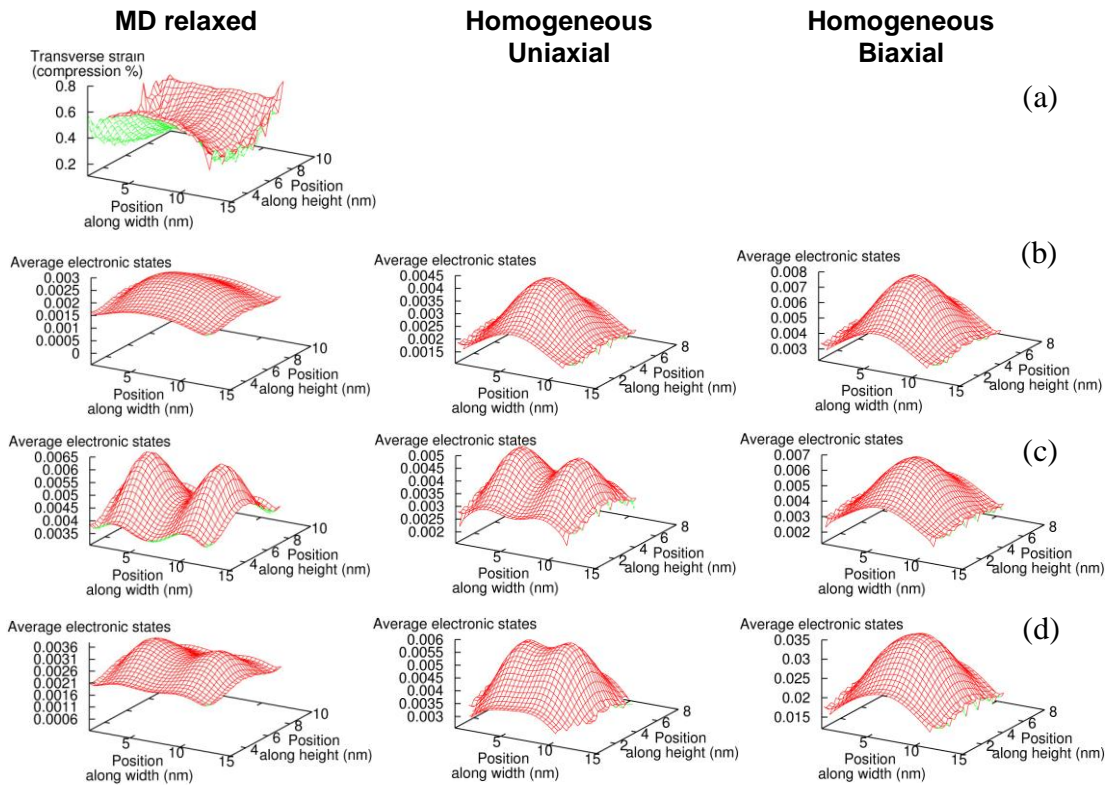
Fig. 5.10 Spatial distribution of (a) the average (over longitudinal direction) transverse strain in the MD relaxed (7,13) Ge wire, (b) the electronic states in the valence band range 0 to -0.02 eV (referenced to VB edge) of the three kinds of (7,13) wire, (c) the the electronic states in the valence band range -0.02 to -0.04 eV, (d) the electronic states in the valence band range -0.04 to -0.06 eV

The discussion in sub-sections 5.3.3 to 5.3.6 indicates that the non-uniformity in strain in the wires causes the valence band edge to shift such that the bandgap decreases and the radius of curvature of the valence band at the edge remains small. But the overall valence bandstructure and the average hole effective mass appear to be influenced largely by the nature of strain in the wires. It also appears from the discussion in this section that because the electronic state distribution in the MD relaxed structures, while being similar to that in either the uniaxial or the biaxial case, does not appear to lie in between those of

the homogeneous uniaxial and biaxial wires, the non-homogenity in the strain could also be having an effect on the observations for the MD relaxed wire. However, it is not very clear at this point whether, besides the average nature of strain, the non-uniformity of strain also has any role to play in the bandstructure properties of the MD relaxed wires.

5.3.8 TB calculations of wires homogeneously strained by average strain in MD relaxed wires
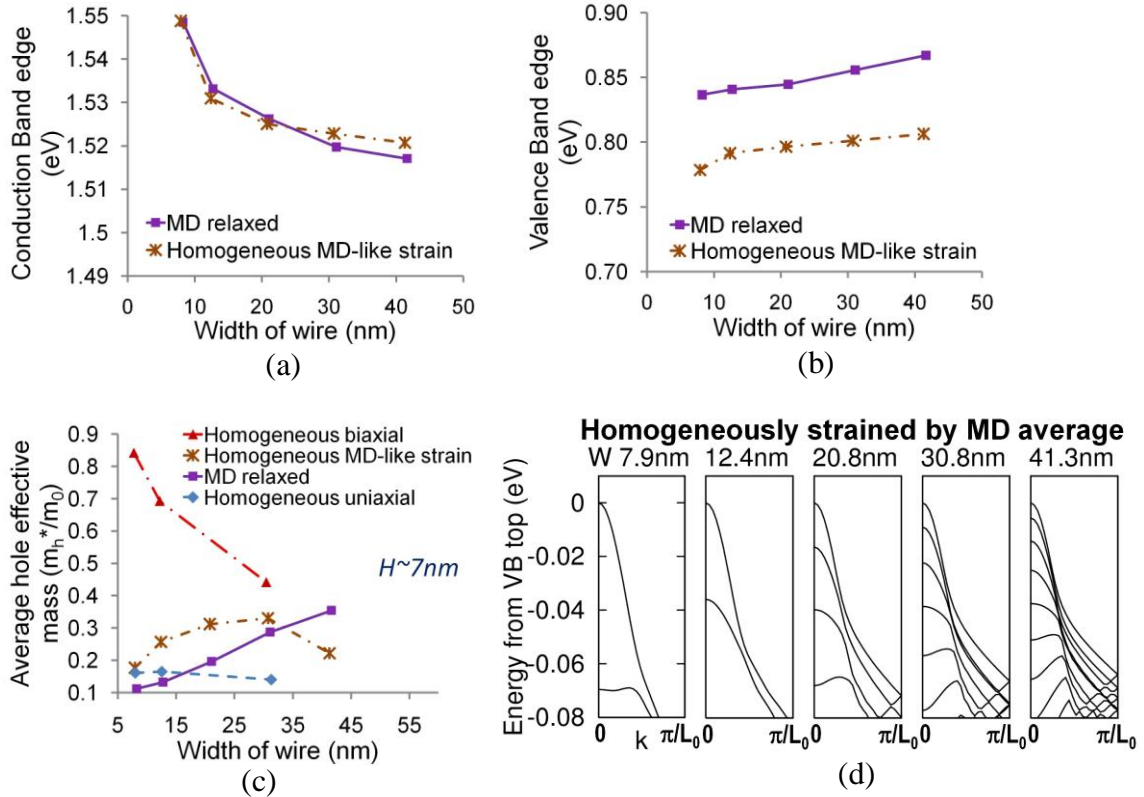
Fig. 5.11 Comparison of the MD relaxed wire with similarly strained homogeneous wire showing (a) the conduction band edge, (b) the valence band edge and (c) the average hole effective mass. (d) The valence bandstructures in the ~7nm high homogeneous wires with strains equal to the average of the corresponding MD relaxed wire

The easiest way to check whether the strain non-uniformity makes any difference is to compare the MD relaxed wires with homogeneously strained wires equivalent to the MD strained wires in their dimensions and average strain. The average strains for the wires being cases in between the extreme cases of purely uniaxial case (to which the small width wires are close) and the biaxial case (to which the higher width wires are close), one would expect the homogeneous wires to exhibit behavior in between these two extreme

cases, and as seen in figure 5.8, this is indeed the case. The homogeneous wires show neither the upward shift in the valence band edge (figure 5.11(b)), nor a monotonous increase in the average hole effective mass with increase in the width of the wire (figure 5.11(c)). The difference between the MD relaxed and the homogeneous wire with similar average strain is also evident from the valence bandstructures shown in fig. 5.11(d). The subbands of the homogeneous 41.3nm wide with average strains similar to the equivalent MD relaxed wire share far more similarity with the subbands of the homogeneous biaxially strained wire than do the subbands of the corresponding MD relaxed wire. In other words, the bandgap reduction, the low hole effective mass (even smaller than the purely homogeneously uniaxial case) for smaller widths or the high effective mass (higher than the purely homogeneously biaxial case) in the MD relaxed wires arise from the non-homogenity of the strain. **These results lead to the conclusion that the non-uniformity of the strain matters in determining the bandstructure properties.** The next two sections study how this dependence on non-homogenity can be understood in terms of the band and effective mass distributions over the bonds strained to different degrees in the MD relaxed wires.

5.3.9 Transverse strain and valence bands in MD relaxed wires

All the wires are compressively strained by about 2% in the longitudinal direction. This means only one of the strains in the other two directions can be considered independent. So, unless otherwise stated, the strain in this and the next section would refer to the transverse strain. Also, all the analysis in this and the next section is dependent on the atomic-level resolution of the tight-binding eigenfunction corresponding to each eigenstate.

Plots, of the kind shown in Fig. 5.12(a) for (7,13) wire, of the electronic states over a given energy range ΔE at the various bonds ij against the strain of bond ij can be obtained for various energy ranges ΔE. From this one could obtain an average electronic state/bond distribution over various strains, as shown by the yellow curve in Fig. 5.12(a) or a total electronic states vs strain distribution for ΔE. Such state distributions indicate the extent to which the states in a given energy range are present at variously strained bonds. The peak, the asymmetry and the steepness of the distributions in such plots can be summed up in peak and FWHM plots. Representatives of such plots are shown in Figs. 5.12(b) and 5.12(c) for various energy ranges (ΔE=0.01eV) of the valence band of (7,13) wire. As can be seen in Figs. 5.12(b), the state per bond distributions are relatively flat

while the total state distributions are relatively sharp, meaning that the states are not selective towards bonds with any particular strains (though the peak is close to the average), and the total state distribution is primarily influenced by the bond distribution over strains shown in figure 5.2. This indicates that even the highly strained bonds in the MD relaxed wire contribute significantly to the states, and as a result, the equivalently sized homogeneous wire with only a single strain would have a different bandstructure, as seen in section 5.3.8. Figure 5.12(d) shows the average strains over the valence bands. It is also interesting to note that on average, the valence band states are shifted to more tensile than average transverse strains for the smaller cross-section and to more compressive than average transverse strains for the larger cross-section wires. All this implies that the non-homogenity of the strain in the realistic wires cannot be ignored.
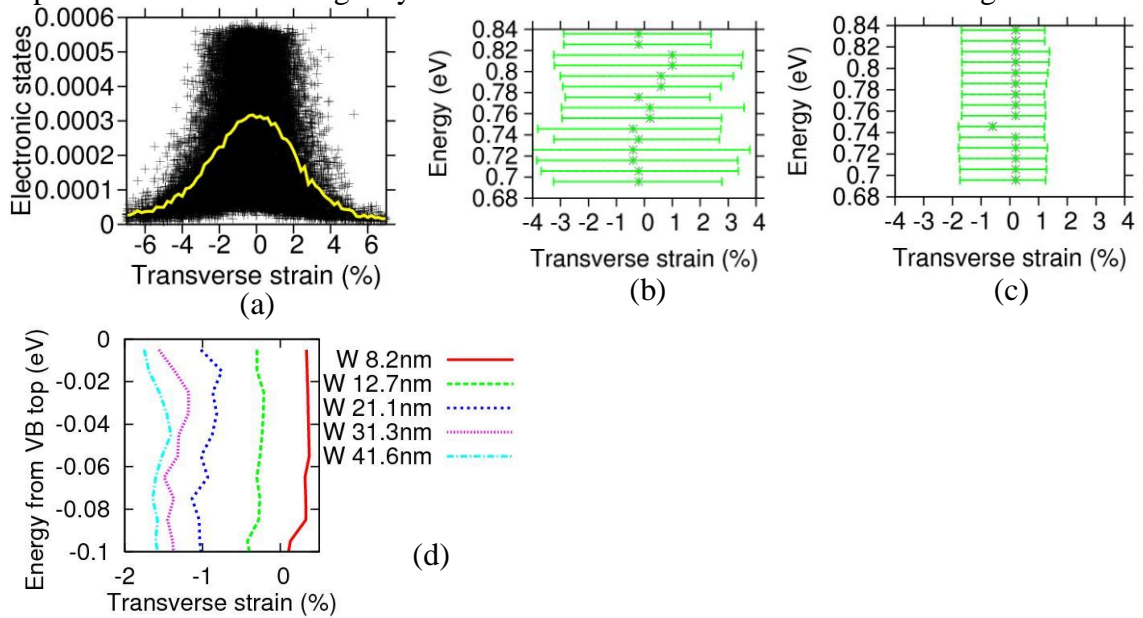
Fig. 5.12 (a) The states contributed by various bonds (black pluses) to the first 0.01 eV of valence bands at the VB edge in the (7,13) MD relaxed wire; the yellow curve shows the average contribution per bond, (b) the peak and the FWHM of the average electronic states per bond versus strain curves similar to the one shown in fig. (a) for the 12.7nm wide wire (the VB edge is at 0.841 eV), (c) the peak and the FWHM of the total electronic states versus strain curves for the 12.7nm wide wire and (d) the average transverse strain at the VB energy states in the MD relaxed (7,W) wires

5.3.10 Transverse strain and hole effective masses in MD relaxed wires

The importance of non-homogeneous strains can also be seen for the effective mass. The individual hole effective mass contributions from the electrons at various atoms can be obtained as:

$$m*_{a}^{-1} = \frac{\sum_{i}\sum_{b_a}\psi_{ib_a}^2 m*_{i}^{-1} e^{-E_i/k_B T}}{\sum_{i} e^{-E_i/k_B T}} \qquad (5.5)$$

where $m*_a^{-1}$ is the inverse effective mass contribution from the states at atom a, $m*_i^{-1}$ is the total inverse effective mass contribution from the state i given by:

$$m*_{i}^{-1} = \frac{1}{\hbar^2}\frac{d^2 E}{dk^2}\bigg|_{i} \qquad (5.6)$$

and the other symbols are as defined earlier in sections 5.3 and 5.3.7, such that the average hole effective mass in the wire is given by $m*$ as:

$$m*^{-1} = \sum_{a} m*_{a}^{-1} \qquad (5.7)$$

Finally, in a manner similar to DOS, the inverse effective mass contribution from the states at bond ij is given by:

$$m*_{ij}^{-1} = \frac{m*_{i}^{-1}}{n_i} + \frac{m*_{j}^{-1}}{n_j} \qquad (5.8)$$


(a)   (b)   (c)
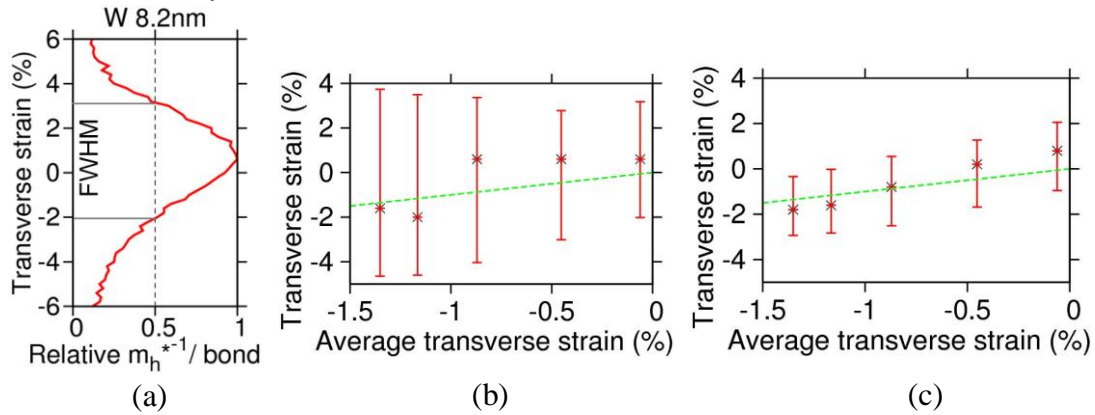
Fig. 5.13 (a) The normalized plot of $m*^{-1}$ contribution per bond at various strains in (7,8) MD relaxed wire, (b) the peak and the FWHM of the $m*^{-1}$ contribution per bond distributions similar to the one shown in fig. a for all MD relaxed wires plotted against their average transverse strain, (c) the peak and the FWHM of the total m_h*^{-1} contribution distributions of the wires

The essential features for the wires are then summed up by peak and FWHM plot. Both the total contribution and the per atom contribution are considered. Once again the total contribution from a particular strain appears to be heavily influenced by the number of bonds such that maximum overall contribution to the effective mass come from strains close to the average. A decrease in selectivity of the strains that contribute the most to the average inverse effective mass is observed as the width of the wires is increased. This means is that for smaller wires the effective mass is heavily contributed by states at the

bonds that are close to average strained but for larger wires, this influence is less selective. This would, as the wire width is increased, diminish the ability to obtain correct effective mass from simulating a homogeneous wire with the same average strain as the MD relaxed wire.

## 5.4 Device (p-type) with strained-Si/strained-Ge/strained-Si nanowire as channel
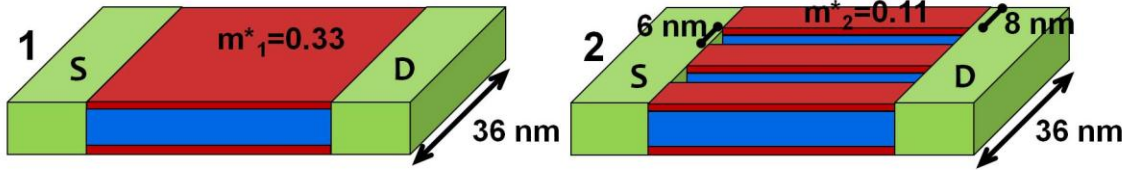
Fig. 5.14 The two cases (1 and 2) of p-type MOSFET device considered in section 5.4. S and D represent source and drain respectively.

This section studies the implications of the results obtained in the previous sections for a p-type transistor. The MOSFET shown in figure 5.14 is considered. In case 1, a single (7,36) heterowire serves as the channel. In case 2, three parallel (7,8) wires replace the single channel in case 1. Both channels (i.e., cases 1 and 2) occupy the same area. The effective mass for the single wire in case 1 is $m*_1=0.33m_0$, while for case 2 , the effective mass of each thin wire is given by $m*_2=0.11m_0$. Assuming an energy-independent relaxation time τ for scattered (diffusive) transport through the wires and a constant value for τ, the transconductances g_m for the ballistic and the scattered transport cases are proportional to half and unity powers of $m*^{-1}$ respectively, as shown below:

$g_m \; \alpha \;\; WC_g v_T \;\;$ *for ballistic* $\qquad g_m \; \alpha \;\; W \bullet (m*)^{-0.5}$ (5.9)

$g_m \; \alpha \;\; WC_g \mu_{eff} \;\;$ *for scattered* $\qquad g_m \; \alpha \;\; \tau \bullet W \bullet (m*)^{-1}$ *for given length* (5.10)

where W is the width of the channel, C_g is the gate capacitance, v_T is the thermal velocity for ballistic transport and μ_{eff} is the effective mobility for scattered transport. So, in the MOSFET shown in fig. 5.14, for the same area of channel we have the transconductance ratio:

$$\frac{g_{m2}}{g_{m1}} = \frac{n_2}{n_1} \bullet \frac{W_2}{W_1} \bullet \left(\frac{m*_2}{m*_1}\right)^{-\alpha}$$ (5.11)

where $\alpha=0.5$ *for ballistic* and $\alpha=1$ *for scattered* and n_1 and n_2 are the number of wires constituting the channel of a transistor in cases 1 and 2 respectively. It must be noted that the factor $\frac{n_2}{n_1} \bullet \frac{W_2}{W_1}$, called here the packing factor, is 1 when the wires in case 2 are lined

up side by side. So in reality, the packing factor is always less than 1. The higher the packing factor, the higher the transconductance improvement by using the parallel wire channel. So to get better transconductances, one would want to pack the wires in the channel as closely as possible. For the dimensions shown in figure, the transconductance ratio turns out to be 1.155 for the ballistic case and 2 for the scattered case (assuming constant relaxation time).

5.5 Conclusions

1. All wires – unstrained as well as strained with compressive 2% strain in longitudinal direction, whether homogeneously uniaxially strained, homogeneously biaxially strained or MD relaxed – show a rising valence band edge and a decreasing bandgap as the wire width is decreased.

2. From bulk→slab→wire, the hole effective mass increases. Similar trend is expected as wire widths of an unstrained or a particular strained wire are reduced and this is indeed the case.

3. For MD relaxed realistic wires with a fixed 2% compressive strain in the longitudinal periodic direction, an opposite trend is obtained in the hole effective mass with change in width. Hole effective mass is seen to improve (decrease) on reduction in wire width.

4. Valence bands in the MD relaxed wires of higher widths become concave upwards faster leading to a degradation in the average hole effective mass even when the VB edge effective mass is close to uniaxial.

5. It is found that the non-homogenity of strain in MD relaxed wires has a role to play in their bandstructure properties, in particular, the valence band edge, the bandgap and the hole effective mass. The non-homogenity is found to make the hole effective mass smaller for small widths and larger for large widths.

6. The influence of non-homogenity can be understood in terms of the large per bond contribution of bonds with strains different from average strains to the valence bands and the effective masses. The net contribution is however concentrated around the average strains of the wires owing to the high population of bonds around the average strain.

7. Several small width s-Si/s-Ge/s-Si nanowires can be tightly packed to provide the channel of a p-type device that possesses high transconductances under ballistic and scattered (with a constant energy-independent relaxation time) transport conditions.

6. TOWARDS ADAPTIVE TIGHT BINDING FOR NON-BULK BONDS

6.1 Why tight binding?

In the last three chapters it was seen that while one could use DFT calculations to investigate the structures and properties of silicon nanotubes, the large size of some realistic structures such as Si-Ge hetero- nanobars makes the use of *ab initio* calculations for such structures impractical owing to the inability of using periodic boundary conditions to model non-periodic structural characteristics such as non-uniform strain or defects. Moreover, as was mentioned in chapter 3, DFT is well known to under-estimate band gaps. The GW correction provides realistic band gaps but is computationally even more expensive. An alternative to these *ab initio* electronic structure methods is provided by the empirical tight binding (TB) method, which can calculate electronic structure for several million atoms. It is for this reason that the size scalable method of tight-binding was used to investigate the electronic properties of the nanobars. However, it is found that this method, in its original form, is unable to simulate arbitrary geometry structures (unless the parameters are re-optimized for the specific geometry). This chapter will investigate adapting tight binding for non-bulk bonding environment in materials and lay the groundwork for future work in fully developing an adaptive tight binding method. While in the long run, this technique is expected to be made most general, the current description will focus on getting reasonably accurate band-structure for non-bulk bonding environments in pure silicon, such as Si surfaces.

One can summarize the merits and demerits of using adaptive tight binding under the following headings:

1. *Generality*: An adaptive tight binding would expected to be more general and transferable than alternative methods like extended Huckel theory. However, not being an *ab initio* method, it would certainly be less general than an *ab initio* method like DFT with GW.

2. *Computational Complexity*: Tight binding is computationally much less involved than an *ab initio* method like GW.

3. *Scalablity*: The computational complexity of *ab initio* methods like GW prohibits their use for larger systems with more than about a 100 atoms. Since most materials and devices have random structural irregularities, use of an *ab initio* method to simulate a periodic model of ~100 atoms such structures does not model the problem realistically. Tight binding allows one to simulate such large systems without any structural approximations.

4. *Compatibility with other methods (e.g. NEGF for transport, molecular dynamics)*: Tight binding model can be used to describe systems for treatment with other techniques for specific characterizations. For example, as described in chapter 1, when simulating transport properties using the NEGF approach, one can use the Hamiltonian from the TB to describe the channel in a nano-scale electronic device in a very simple fashion such that a large device can be simulated with computational ease.

6.2 Case study – Si (100) surface

The transferability of the $sp^3d^5s^*$ orthogonal TB parameters [20, 21, 50] fitted for bulk Si to non bulk-like bonds has to be investigated first if TB is to be used for strongly deformed nano-scale structures. The easiest test bed for this investigation is the reconstructed Si (100) surface, which is also of practical utility.

6.2.1 Surfaces/ interfaces and electronic devices

In the last three chapters, it was seen that in 1-D nanostructures, surfaces become so important that they can drive changes in the underlying material geometry, either by, as in the case of silicon nanotubes, making it highly non-bulk, thereby leading to novel properties or, as in case of Si-Ge nanobars, causing significant strain changes in the underlying bulk geometry.

That surfaces, interfaces and other non-bulk or non-ideal bonding environments like defects in the material play an important role in the behavior of semiconductor electronic devices was recognized during the early stages of microelectronics industry. Change in the threshold voltage of MOS and Fermi level pinning at metal-semiconductor interface are two among well-known effects of interfacial geometries and conditions on device behavior. The effect of interface properties on device behavior has also been

observed in SiNW FETs in a fashion similar to the conventional MOSFET. Detrimental effects of particles or chemical contamination sitting on surfaces or interfaces on device performance and reliability is one of the reasons for wafer cleaning processes constituting 30-40% of the steps in the total manufacturing process. Just like for the devices, as the interconnect size scales down, the impact of interconnect sidewalls and surface roughness on signal propagation increases. While the front-end engineering endeavors to control the surface and interfacial structure of devices during fabrication, non-ideal environments are unavoidable. Simulations not only help in understanding the detrimental effects of the non-bulk bond environments on device behavior but also in designing devices where such non-bulk bonds can be put to use to achieve desirable properties. For example, open surface leads to gap states which affect transport characteristics of 1-D nano structures by providing extra "stepping stones" for electrons in the band gap.

6.2.2 DFT-GGA simulations of silicon (100) slab

Of the several possible reconstructions of the Si (100) surface, the symmetrical p(2X1)s and the asymmetrical p(2X1)a (fig 6.1(a)) are among the most likely.[55, 56] We carried out the DFT-GGA relaxation of Si slab in SeqQuest,[33] reconstructed on both surfaces, first symmetrically then asymmetrically. Three thicknesses of the slab were simulated as shown in fig 6.1(c). For example, 32 monolayers is equivalent to eight bulk (110) unit cells and for this thickness the surface energies w.r.t. Si bulk were:

Symmetric: 2.66711 eV/ dimer,   Asymmetric: 2.51076 eV/ dimer

As already known, the p(2X1)a surface is found to be energetically more favorable than the p(2X1)s surface by about 0.16 eV per dimer. The 9 monolayer thick slab in which the dimer bonds on the two opposite surfaces lie perpendicular to each other was also simulated. It is found that the mutual orientation of the surface bonds on the two opposite surfaces affects the energy of the slab very little.

The energetics of the 32 monolayer slab using DFT-GGA when Hydrogen passivated were also studied. One point to note here is that the H atoms arrange themselves symmetrically w.r.t. to the two atoms of the surface dimer and as a result, the surface dimer loses its asymmetric character when H passivated. Fig 6.2 shows the energy of the H passivated structure when the passivation is carried out with 2 H atoms per Si surface dimer, 3 H atoms per dimer and 4 H atoms per dimer. The results are shown in figure 6.2 and indicate that the reconstructed+ passivated surface (2 H atoms per Si surface dimer) is energetically the most stable of the three.
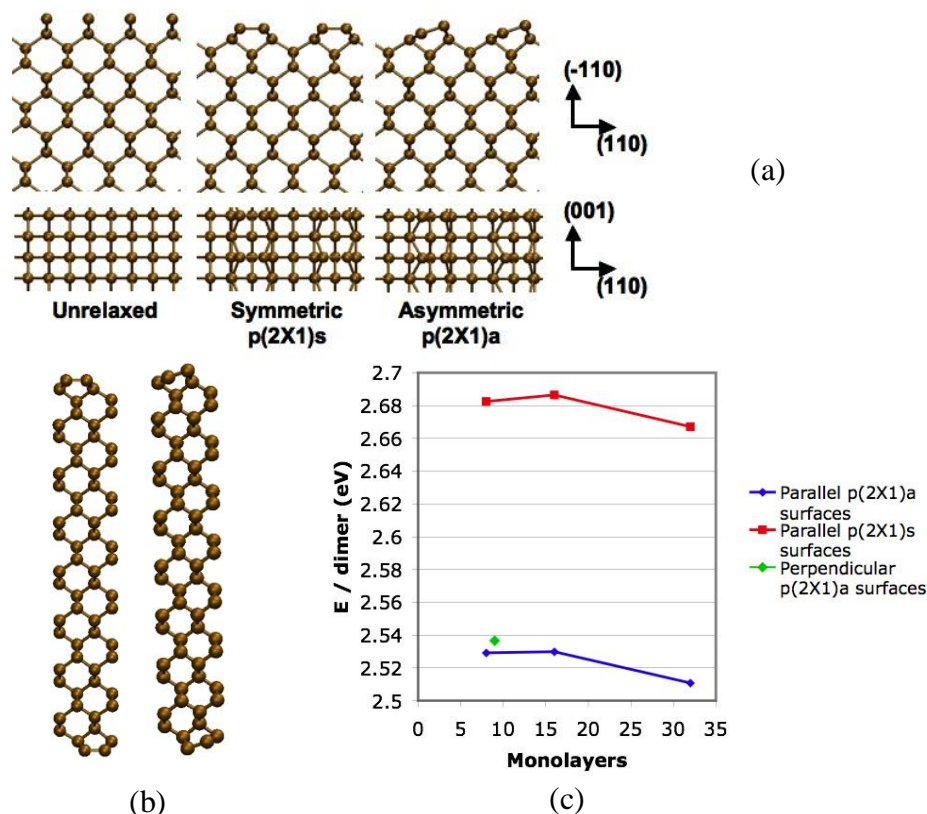
Fig 6.1 (a) The unrelaxed, symmetrically reconstructed p(2X1)s and asymmetrically reconstructed p(2X1)a Si(100) surface. (b) A unit each of 32 monolayer symmetric and asymmetric Si (100) slab simulated (c) Surface energy per dimer for the various thicknesses of the symmetric and asymmetric slabs. The green diamond represents the energy of 9 monolayer p(2X1)a slab which has bonds in mutually orthogonal directions on the two surfaces.
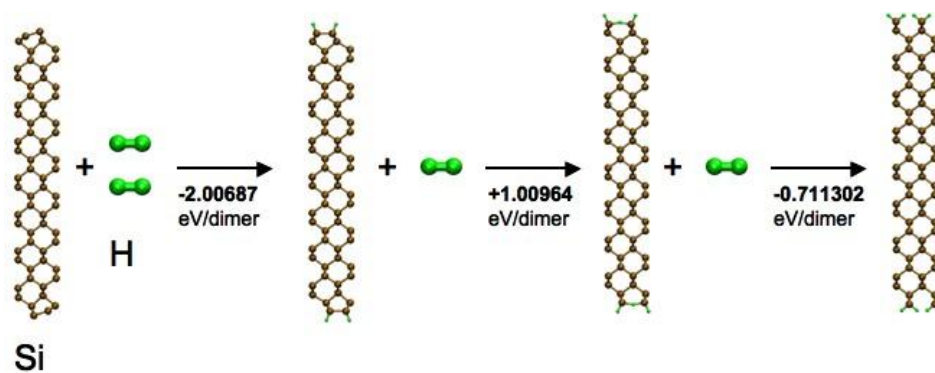

Fig 6.2 Hydrogen passivation of Si (100) surface, showing configurations with two H atoms per Si dimer, three H atoms per Si dimer and 4 Si atoms per Si dimer.

6.3 Simulating Si (100) slab using orthogonal sp³d⁵s* tight binding

To carry out tight binding electronic structure calculations, the NanoElectronics Modeling-3D (NEMO-3D) program [51] is used.
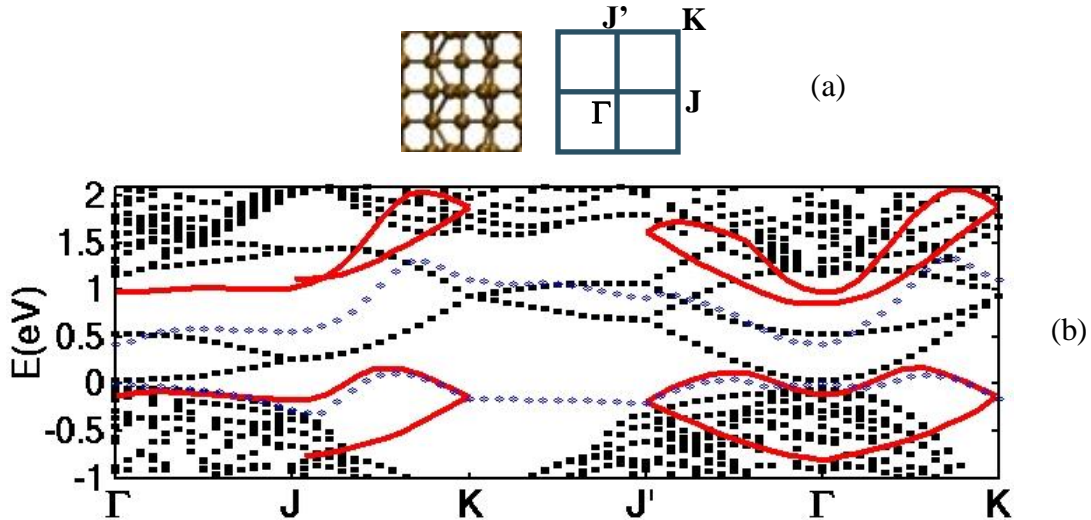

Fig 6.3 (a) The real space unit cell and k-space Brillouin zone of Si (100) surface (b) Band structure (black squares) from sp³d⁵s* tight binding (NEMO-3D) of 32 monolayer thick Si (100) slab when the geometry and connectivity of unrelaxed bulk surface is retained. The red curves constitute the surface states of p(2X1)a surface obtained in ref. 43 from GW and the blue dots are the DFT-LDA results.

6.3.1 Simulating bulk geometry slab without connectivity modification

The original version of NEMO-3D has the capability to simulate several different bulk geometries and needs modification to be able to simulate any arbitrary geometry. As seen in figure 6.3, if the connectivity of the bulk is retained and the dangling bonds left on the surface, the bandstructure obtained from NEMO3D with sp³d⁵s* bulk parameters has no similarity with the DFT-LDA and GW results for p(2X1)a surface.

6.3.2 Simulation with proper connectivity

Modifying the code to include proper geometry and connectivity results in a band structure for the p(2X1)a surface where the gap states (surface states) are close to the GW result qualitatively and in terms of curvatures but shifted in energy by about 0.5 eV. We obtain a band gap of 0.304 eV from the bulk TB parameters while the GW band gap is 0.65 eV.[57] The TB band gap is still better than the LDA band gap of 0.25 eV. We also

note that the p(2X1)s surface is metallic, which is a well-known result for symmetrically dimerized Si (100) surface.


(a)

(b)

(c)
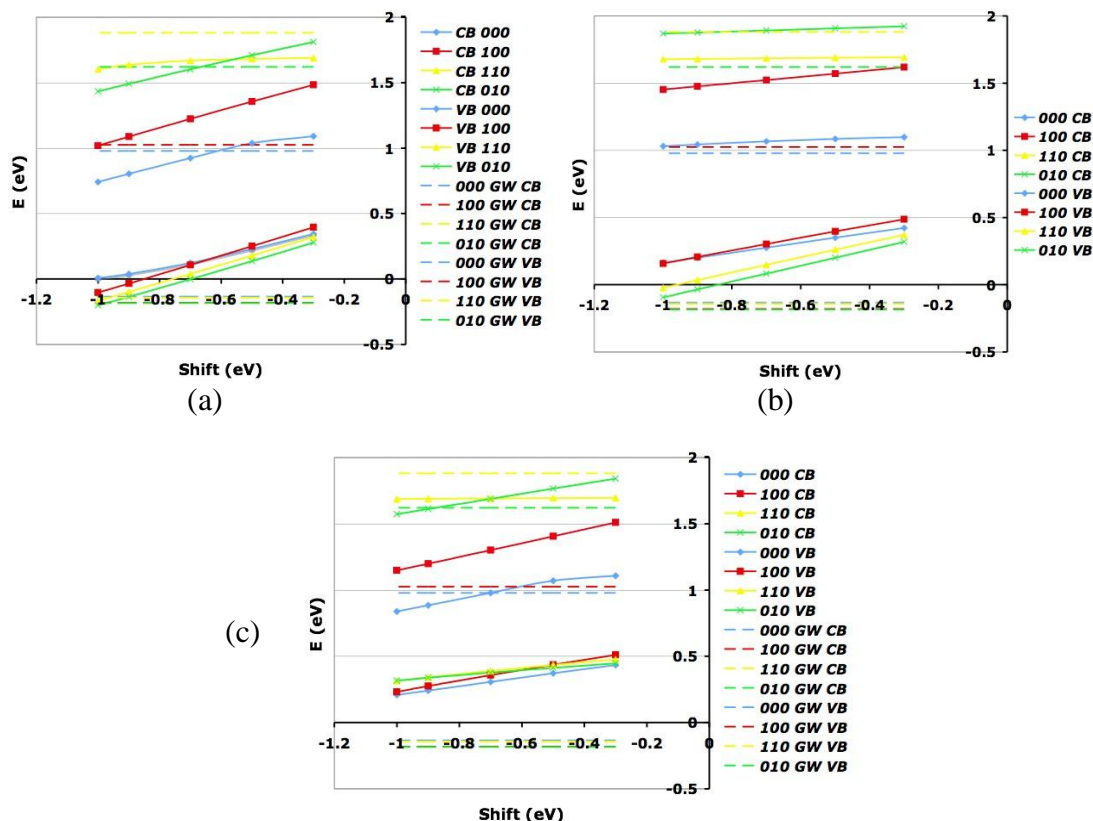
Fig 6.4 Self-orbital parameter shifts for surface dimer atoms versus the energy of valence band (VB) and conduction band (CB) edges at symmetry points [k_x is scaled by 2 and k_y by 4 in the points reported in the figures] when (a) the inner atom parameters are shifted, (b) the outer atom parameters are shifted, (c) both inner and outer dimer atom parameters are shifted by the same amount

6.3.3 Modifying orbital self parameters for surface atoms

To match the TB results to the GW results, the self-orbital parameters (figs 6.4 (a)-(c) for change of -1eV) were modified and the effects on the energies at the ends of each section of the traced k-path were observed. The dotted lines represent the GW bands. It is seen that changing the outer atom self parameters mostly affects the valence band. Shifting the orbital self parameters for both the surface atoms by -1 eV brings the band-structure close to the GW result (figure 6.5) and is a substantial improvement over the LDA result. Thus the parameter modification to adjust to new bond environments is found to be promising.
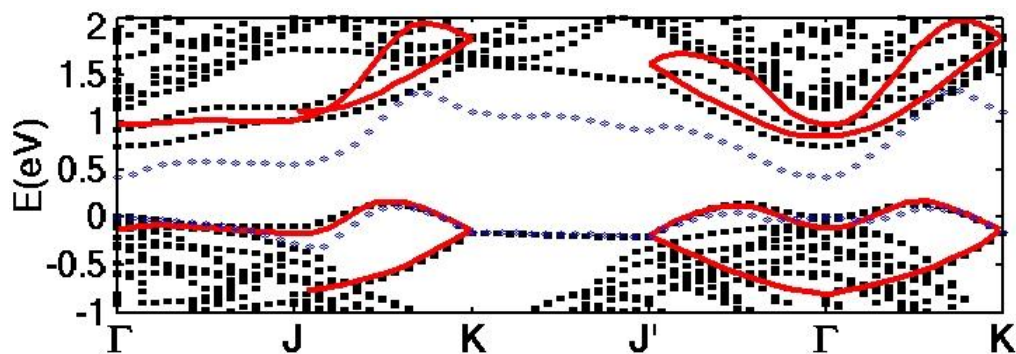
Fig 6.5 Band structure (black squares) from sp^{3}d^{5}s* tight binding (NEMO-3D) of 32 monolayer thick Si (100) slab when the self-orbital parameters of all surface atoms are shifted by -1eV. The red curves constitute the surface states obtained in ref. 37 from GW and the blue dots are the DFT-LDA results.

6.3.4 Simulating local density of surface states
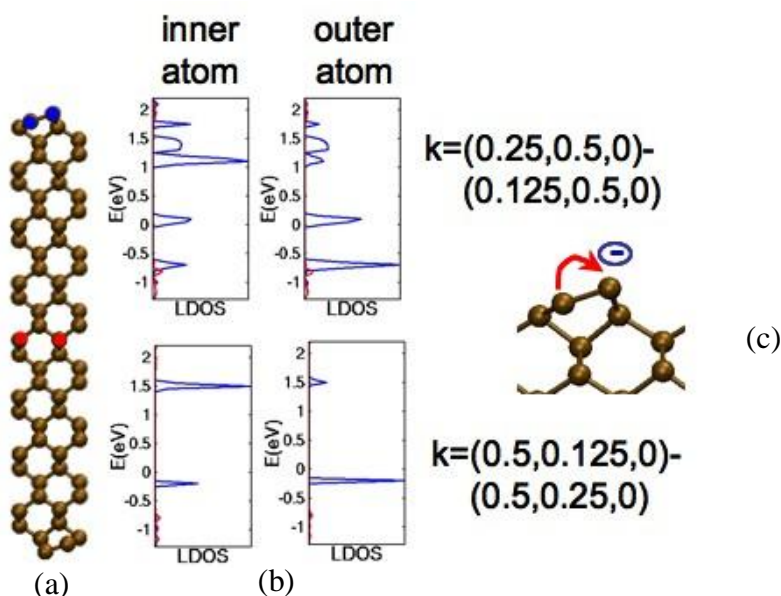
Fig 6.6 (a) Surface atoms (blue) and bulk atoms (red) for which LDOS are calculated, (b) the LDOS for the inner and outer surface atoms over two different k paths (c) the LDOS are explained by the transfer of e- from the inner atom to the outer atom

Using the parameter shifts that led to the bandstructure shown in fig. 6.5, the local density of states for the two dimer atoms on the Si (100) slab surface and corresponding bulk atoms were obtained for two ranges of k points (see figure 6.6). The following are the important points from this figure:

The bulk atoms (those that are far away from the surface) do not contribute to the states in the gap (the so-called π and π* states).

The lower state in the gap (π or the filled bonding state) sits mostly on the outer atom of the dimer, while the upper surface state (π^* or the unfilled anti-bonding state) sits mostly on the inner atom. This implies charge asymmetry and the transfer of electrons from the inner to the outer atom in the asymmetric dimer (referred to as Jahn-Teller effect in literature).

6.4 Towards adaptive tight binding

The above results can be understood in light of what is known about the Slater-Koster model [18] of orthogonal tight binding. In chapter 2, it was mentioned that the parameters for empirical TB come from fitting to experimental or *ab initio* data for a given structure, and the orthogonal sp^{3}d^{5}s* parameters used in this thesis, in particular, come from genetic algorithm optimization to fit band edges and effective masses of *ab initio* band-structure of bulk Si or bulk Ge at symmetry k points (Klimeck *et al.*[19, 20]). It was also clear in chapter 2 that Slater-Koster formulae [18] (equations) allow the use of a common space reference to represent the atomic orbitals of all atoms in the system by the adaptation of the parameters to the universal axes rigidly rotated with respect to the axes associated with the individual bonds. The basic bond parameters are unmodified and uniform over all bonds. In other words, the Slater-Koster TB approach, while it allows application of bulk parameters to a bond oriented in any direction, it does not describe the evolution of the bond parameters when the bond environment changes (i.e., when every bond in the structure does not see the same spatial symmetry, number of nearest neighbors, bond lengths or bond angles). The modification in bond lengths, only for small strains (<9%) is handled reasonably well by the method described by Boykin *et al.*[21] But the sp^{3}d^{5}s* orthogonal TB parameters fitted for bulk Si are not directly applicable to non bulk-like bonds since any change in the connectivity and bond angles would affect the Hamiltonian and hence the TB parameters.

The good results obtained for silicon surface from tight binding by a very simple modification to the surface atom parameters promise applicability of tight binding to surfaces and perhaps other non-bulk bond environments. One could then envision an adaptive tight binding. The basic idea of adaptive TB is to tweak the bulk parameters for non-bulk bond environments. The major dependencies that should be considered first include the coordination number (number of bonds) and the bond angles for each atom both of which modify the symmetry properties of the atom w.r.t. those in the bulk. To

begin with, it can be assumed that for the bond strains involved the parameter modifications suggested by Boykin *et al.* [21] hold good. Thus if the original parameter on an atom is represented by P_m, the co-ordination number (number of bonds) of the atom by n and the bond angles by α_i (i=1 to n), the new parameter P_m' in adaptive tight binding is given by:

$$P_m' = f(P_m, n, \alpha_1, \alpha_{2,...} \alpha_n)$$
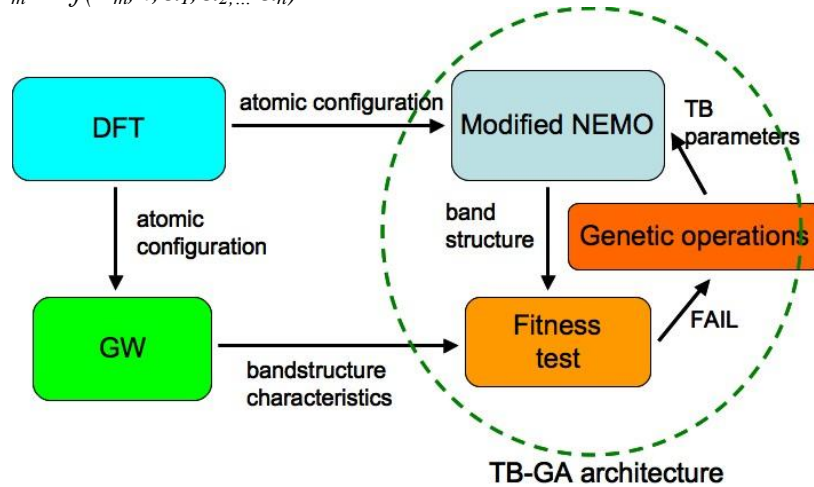
Fig 6.7 Flowchart depicting the process of finding optimal parameters for adaptive tight binding using genetic algorithms

First, the optimal P' would be obtained using an optimization procedure (genetic algorithms) for reasonably enough cases of n and α_i. The function f can then be represented in some Hilbert space (e.g. power series) by finding coefficients to a certain order in the linear combination of the basis functions for the least mean square error of f from the data P_m' versus $(n, \alpha_1, \alpha_{2,...} \alpha_n)$.

Figure 6.7 shows the full scheme of obtaining the optimal set of parameters for the Si(100) slab from genetic algorithm. The bond angles of the dimer atoms on the surface would be swept and the optimal TB parameters for each case of bond angles fitted to the GW bandstructure using genetic algorithms by the loop shown in figure 6.7. Then the function f for each parameter P_m would be obtained using the method described above.

LIST OF REFERENCES

LIST OF REFERENCES

[1]   L. A. Ponomarenko*, et al.*, "Chaotic dirac billiard in graphene quantum dots," *Science,* vol. 320, pp. 356-358, Apr 2008.

[2]   G. S. Snider and R. S. Williams, "Nano/CMOS architectures using a field-programmable nanowire interconnect," *Nanotechnology,* vol. 18, Jan 2007.

[3]   News Release. *Hybrid nano-CMOS chips could be far denser, but cooler.* Available: http://www.hp.com/hpinfo/newsroom/press/2007/070116a.html

[4]   ITRS. *International Technology Roadmap for Semiconductors 2007.* Available: http://www.itrs.net/links/2007itrs/home2007.htm

[5]   Y. Wu*, et al.*, "Controlled growth and structures of molecular-scale silicon nanowires," *Nano Letters,* vol. 4, pp. 433-436, Mar 2004.

[6]   Y. Cui*, et al.*, "Doping and electrical transport in silicon nanowires," *Journal of Physical Chemistry B,* vol. 104, pp. 5213-5216, Jun 2000.

[7]   A. B. Greytak*, et al.*, "Growth and transport properties of complementary germanium nanowire field-effect transistors," *Applied Physics Letters,* vol. 84, pp. 4176-4178, May 2004.

[8]   D. W. Wang*, et al.*, "Silicon p-FETs from ultrahigh density nanowire arrays," *Nano Letters,* vol. 6, pp. 1096-1100, Jun 2006.

[9]   Y. Wu*, et al.*, "Single-crystal metallic nanowires and metal/semiconductor nanowire heterostructures," *Nature,* vol. 430, pp. 61-65, Jul 2004.

[10]   Y. Cui and C. M. Lieber, "Functional nanoscale electronic devices assembled using silicon nanowire building blocks," *Science,* vol. 291, pp. 851-853, Feb 2001.

[11]   J. Hahm and C. M. Lieber, "Direct ultrasensitive electrical detection of DNA and DNA sequence variations using nanowire nanosensors," *Nano Letters,* vol. 4, pp. 51-54, Jan 2004.

[12]   A. I. Hochbaum and P. D. Yang, "Semiconductor Nanowires for Energy Conversion," *Chemical Reviews,* vol. 110, pp. 527-546, Jan 2010.

[13]   P. L. McEuen*, et al.*, "Single-walled carbon nanotube electronics," *Ieee Transactions on Nanotechnology,* vol. 1, pp. 78-85, Mar 2002.

[14]   J. Xiang*, et al.*, "Ge/Si nanowire heterostructures as high-performance field-effect transistors," *Nature,* vol. 441, pp. 489-493, May 2006.

[15]   P. Hashemi*, et al.*, "Asymmetric strain in nanoscale patterned strained-Si/strained-Ge/strained-Si heterostructures on insulator," *Applied Physics Letters,* vol. 91, Aug 2007.

[16]   Y. Park*, et al.*, "Strain relaxation in Si/Ge/Si nanoscale bars from molecular dynamics simulations," *Journal of Applied Physics,* vol. 106, Aug 2009.

[17]   A. C. T. van Duin*, et al.*, "ReaxFF: A reactive force field for hydrocarbons," *Journal of Physical Chemistry A,* vol. 105, pp. 9396-9409, Oct 2001.

[18]   J. C. Slater and G. F. Koster, "SIMPLIFIED LCAO METHOD FOR THE PERIODIC POTENTIAL PROBLEM," *Physical Review,* vol. 94, pp. 1498-1524, 1954.

[19]   G. Klimeck*, et al.*, "Si tight-binding parameters from genetic algorithm fitting," *Superlattices and Microstructures,* vol. 27, pp. 77-88, Feb-Mar 2000.

[20]   T. B. Boykin*, et al.*, "Valence band effective-mass expressions in the sp(3)d(5)s(*) empirical tight-binding model applied to a Si and Ge parametrization," *Physical Review B,* vol. 69, Mar 2004.

[21]   T. B. Boykin*, et al.*, "Diagonal parameter shifts due to nearest-neighbor displacements in empirical tight-binding theory," *Physical Review B,* vol. 66, Sep 2002.

[22]   D. Ma*, et al.*, "Small-diameter silicon nanowire surfaces," *SCIENCE,* vol. 299, pp. 1874-1877, MAR 21 2003 2003.

[23]   C. X. Wang*, et al.*, "Origin of diameter-dependent growth direction of silicon nanowires," *Nano Letters,* vol. 6, pp. 1552-1555, Jul 2006.

[24]   B. Marsen and K. Sattler, "Fullerene-structured nanowires of silicon," *Physical Review B,* vol. 60, pp. 11593-11600, Oct 1999.

[25]   R. Kagimura*, et al.*, "Structures of Si and Ge nanowires in the subnanometer range," *Physical Review Letters,* vol. 95, Sep 2005.

[26]   J. Bai*, et al.*, "Metallic single-walled silicon nanotubes," *Proceedings of the National Academy of Sciences of the United States of America,* vol. 101, pp. 2664-2668, Mar 2004.

[27]   I. Ponomareva*, et al.*, "Structure, stability, and quantum conductivity of small diameter silicon nanowires," *Physical Review Letters,* vol. 95, Dec 2005.

[28]   A. Palaria*, et al.*, "Structures and energetics of silicon nanotubes from molecular dynamics and density functional theory," *Physical Review B,* vol. 78, Nov 2008.

[29]   A. C. T. van Duin*, et al.*, "ReaxFF(SiO) reactive force field for silicon and silicon oxide systems," *Journal of Physical Chemistry A,* vol. 107, pp. 3803-3811, May 2003.

[30]   B. J. Lee and M. I. Baskes, "Second nearest-neighbor modified embedded-atom-method potential," *Physical Review B,* vol. 62, pp. 8564-8567, Oct 2000.

[31]   M. J. Buehler*, et al.*, "Multiparadigm modeling of dynamical crack propagation in silicon using a reactive force field," *Physical Review Letters,* vol. 96, Mar 2006.

[32]   J. P. Perdew*, et al.*, "Generalized gradient approximation made simple," *Physical Review Letters,* vol. 77, pp. 3865-3868, Oct 1996.

[33]   P. A. Schultz. *SEQQUEST Project*. Available: http://dft.sandia.gov/Quest

[34]   M. Zhang*, et al.*, "Why silicon nanotubes stably exist in armchair structure?," *Chemical Physics Letters,* vol. 379, pp. 81-86, Sep 2003.

[35]   B. Lee and R. E. Rudd, "First-principles calculation of mechanical properties of Si(001) nanowires and comparison to nanomechanical theory," *Physical Review B,* vol. 75, May 2007.

[36]   L. H. Shi*, et al.*, "Size dependent thermoelectric properties of silicon nanowires," *Applied Physics Letters,* vol. 95, Aug 2009.

[37]   L. H. Liang and B. W. Li, "Size-dependent thermal conductivity of nanoscale semiconducting systems," *Physical Review B,* vol. 73, 2006.

[38]   X. Zhao*, et al.*, "Quantum confinement and electronic properties of silicon nanowires," *PHYSICAL REVIEW LETTERS,* vol. 92, pp. -, JUN 11 2004 2004.

[39]   T. Akiyama*, et al.*, "Structures and electronic properties of Si nanowires grown along the [110] direction: Role of surface reconstruction," *SURFACE SCIENCE,* vol. 602, pp. 3033-3037, SEP 15 2008 2008.

[40]   A. K. Singh*, et al.*, "Pristine semiconducting 110 silicon nanowires," *Nano Letters,* vol. 5, pp. 2302-2305, Nov 2005.

[41]   *The ABINIT code is a common project of the Université Catholique de Louvain, Corning Incorporated, and other contributors.* Available: http://www.abinit.org

[42]   A. Palaria*, et al. ABINIT on nanoHUB*. Available: http://nanohub.org/resources/ABINIT

[43]   H. A. Jahn and E. Teller, "Stability of polyatomic molecules in degenerate electronic states. I. Orbital degeneracy," *Proceedings of the Royal Society of London Series a-Mathematical and Physical Sciences,* vol. 161, pp. 220-235, Jul 1937.

[44]   D. J. Chadi, "ATOMIC AND ELECTRONIC-STRUCTURES OF RECONSTRUCTED SI(100) SURFACES," *Physical Review Letters,* vol. 43, pp. 43-47, 1979.

[45]   F. Yuan*, et al.*, "Mechanically strained Si-SiGeHBTs," *Ieee Electron Device Letters,* vol. 25, pp. 483-485, 2004.

[46]   S. Persson*, et al.*, "Strained-Silicon Heterojunction Bipolar Transistor," *Ieee Transactions on Electron Devices,* vol. 57, pp. 1243-1252, 2010.

[47]   R. People, "PHYSICS AND APPLICATIONS OF GEXSI1-X/SI STRAINED-LAYER HETEROSTRUCTURES," *Ieee Journal of Quantum Electronics,* vol. 22, pp. 1696-1710, Sep 1986.

[48]   E. Wang*, et al.*, *Quantum mechanical calculation of hole mobility in silicon inversion layers under arbitrary stress*, 2004.

[49]   S. E. Thompson*, et al.*, "Future of strained Si/Serniconductors in nanoscale MOSFETs," in *2006 International Electron Devices Meeting, Vols 1 and 2*, 2006, pp. 415-418.

[50]   S. Lee*, et al.*, "Boundary conditions for the electronic structure of finite-extent embedded semiconductor nanostructures," *Physical Review B,* vol. 69, Jan 2004.

[51]   G. Klimeck*, et al.*, "Development of a nanoelectronic 3-D (NEMO 3-D) simulator for multimillion atom simulations and its application to alloyed quantum dots," *Cmes-Computer Modeling in Engineering & Sciences,* vol. 3, pp. 601-642, Oct 2002.

[52]   M. V. Fischetti and S. E. Laux, "Band structure, deformation potentals, and carrier mobility in strained Si, Ge, and SiGe alloys," *Journal of Applied Physics,* vol. 80, pp. 2234-2252, Aug 1996.

[53]   A. Rahman*, et al.*, "Novel channel materials for ballistic nanoscale MOSFETs-bandstructure effects," in *Ieee International Electron Devices Meeting 2005, Technical Digest*, 2005, pp. 615-618.

[54] J. Wang*, et al.*, "Bandstructure and orientation effects in ballistic Si and Ge nanowire FETs," in *Ieee International Electron Devices Meeting 2005, Technical Digest*, 2005, pp. 537-540.

[55] R. A. Wolkow, "DIRECT OBSERVATION OF AN INCREASE IN BUCKLED DIMERS ON SI(001) AT LOW-TEMPERATURE," *Physical Review Letters,* vol. 68, pp. 2636-2639, Apr 1992.

[56] A. Ramstad*, et al.*, "THEORETICAL-STUDY OF THE SI(100) SURFACE RECONSTRUCTION," *Physical Review B,* vol. 51, pp. 14504-14523, May 1995.

[57] M. Rohlfing*, et al.*, "EFFICIENT SCHEME FOR GW QUASI-PARTICLE BAND-STRUCTURE CALCULATIONS WITH APPLICATIONS TO BULK SI AND TO THE SI(001)-(2X1) SURFACE," *Physical Review B,* vol. 52, pp. 1905-1917, Jul 1995.

VITA

VITA

Amritanshu ('Amrit') Palaria holds a Bachelor of Technology degree in Electronics Engineering from India and a Master of Science (thesis) in Electrical and Computer Engineering from the University of Arizona. His research interest lies in the areas of physics of materials applied to electronics or other emerging applications, quantum physics and chemistry and electronic circuits.